TÜBİTAK

Turkish Journal of Earth Sciences

http://journals.tubitak.gov.tr/earth/

Research Article

Turkish J Earth Sci
(2022) 31: 178-192

doi:10.3906/yer-2110-20

Growth of the imbrication zone along the southeast Anatolian orogenic belt: evidence from fission track thermochronology from Gölbaşı region (SE Turkey)

Yusuf TOPAK *

Department of Mining and Mineral Extraction, Adıyaman University, Adıyaman, Turkey

Received: 26.10.2021 • **Accepted/Published Online:** 02.03.2022 • **Final Version:** 29.03.2022

Abstract: One of the major components of continental collision zones is their imbricated zones. Such a zone along the Southeast Anatolian Orogenic Belt (SAOB) is solely controlled by a still-active convergence and accretion system between the Anatolian Plate and Arabian platform since at least Late Cretaceous. The zone is characterized by NEE/SWW-trending, northward-dipping thrust slices that are squeezed between the Tauride Block to the north and the Arabian platform to the south. The units cropping out within the zone comprise Neo-Tethys-related magmatic, ophiolitic, sedimentary and metamorphic rocks with Late Cretaceous to Miocene formation/metamorphism ages. The Karanlıkdere granitoid intrudes into Late Cretaceous Meydan ophiolite, Helete volcanics, and Malatya metamorphics. These units thrust over Cenozoic volcanic and sedimentary rocks. Although various scenarios have been proposed for the late Cretaceous to Neogene evolution of the complex region, quantitative data aiming to understand the growth mechanism of the imbrication zone in the region are limited. The zircon U-Pb and the apatite fission track (AFT) thermochronology were applied to the Karanlıkdere granitoid within the imbrication zone of the Southeast Anatolian Orogenic Belt (SAOB). The LA-ICP-MS zircon U-Pb age yields 79.67 ± 0.24 Ma with 0.23–0.65 Th/U ratios. This age is slightly younger than the previously published ages, indicating that the main body of the Karanlıkdere granitoid formed 3-4 Ma later than the small dikes intruded into other units. The AFT ages are directly controlled by altitude and range between 40.38 ± 3.4 Ma and 22.81 ± 0.63 Ma. The oldest AFT age has the highest altitude, whereas the youngest has the lowest height. The age-temperature models show a slow uplift rate between 40 Ma and 22 Ma. The results indicate that the growth of the imbrication zone in front of the Nappes of the SAOB continued in a steady-state mode with a slow uplift rate of 0.02 ± 0.005 mm/a, during middle-late Eocene to early Miocene and increasing uplift rate during early-middle Miocene, which might be explained by continental collision during early-middle Miocene.

Key words: Southeast Anatolian Orogenic Belt, imbrication zone, Karanlıkdere granitoid, apatite fission track, uplift, Gölbaşı

1. Introduction

The signs of Alpine-Himalayan orogeny in the Anatolian peninsula are manifested by the amalgamation of several microcontinents, split by different branches of the Neo-Tethyan Ocean. The main branch of the Neo-Tethyan Ocean in the region is the northern branch which separates the Eurasian Plate (Pontides) and the Gondwana Anatolide-Tauride Block (Şengör and Yılmaz, 1981). The Inner Tauride Ocean in the center splits the Gondwana-origin microplate, the Kırşehir Block, from the Anatolide-Tauride Block (Görür et al., 1984; 1998). Finally, the southern branch of the Neo-Tethyan Ocean separates the Anatolide-Tauride Block from the Afro-Arabian plates (Şengör and Yılmaz, 1981; Göncüoğlu and Turhan, 1984; Yılmaz, 1993; Okay and Tüysüz, 1999; Bozkurt and Mittwede, 2001; Robertson et al., 2012; Hinsbergen et al., 2016; Karaoğlan et al., 2016; Göncüoğlu, 2019).

The progressive demise of the southern branch of the Neo-Tethyan Ocean beneath the Tauride-Anatolide platform in a north-dipping tectonic environment caused several collision events, including arc-continent and continent-continent collisions during Late Cretaceous-Miocene (Şengör and Yılmaz, 1981; Yılmaz, 1993; Oberhänsli et al., 2010; Oberhänsli et al., 2012; Oberhänsli et al., 2014; Ural et al., 2015; Karaoğlan et al., 2016; Yılmaz, 2019). This tectonic environment formed the Southeast Anatolian Orogenic Belt (SAOB) along the Bitlis-Zagros Suture Zone (Figure 1). The major tectonic units of the SAOB consist of the Arabian platform to the south and the nappe zone to the north, whereas a zone of imbrication formed in between these two units during the late Cretaceous-Miocene. These three zones are separated from each other by major thrusts (Yılmaz, 1993; Yılmaz et al., 1993; Yılmaz, 2019) (Figure 1).

The zone of imbrication formed a narrow (1 to 5 km) east-west trending belt. The zone hosts late Cretaceous-early Miocene deposits participating in the imbrication during and/or after their sedimentation (Yılmaz, 1993;

* Correspondence: ytopak@adiyaman.edu.tr

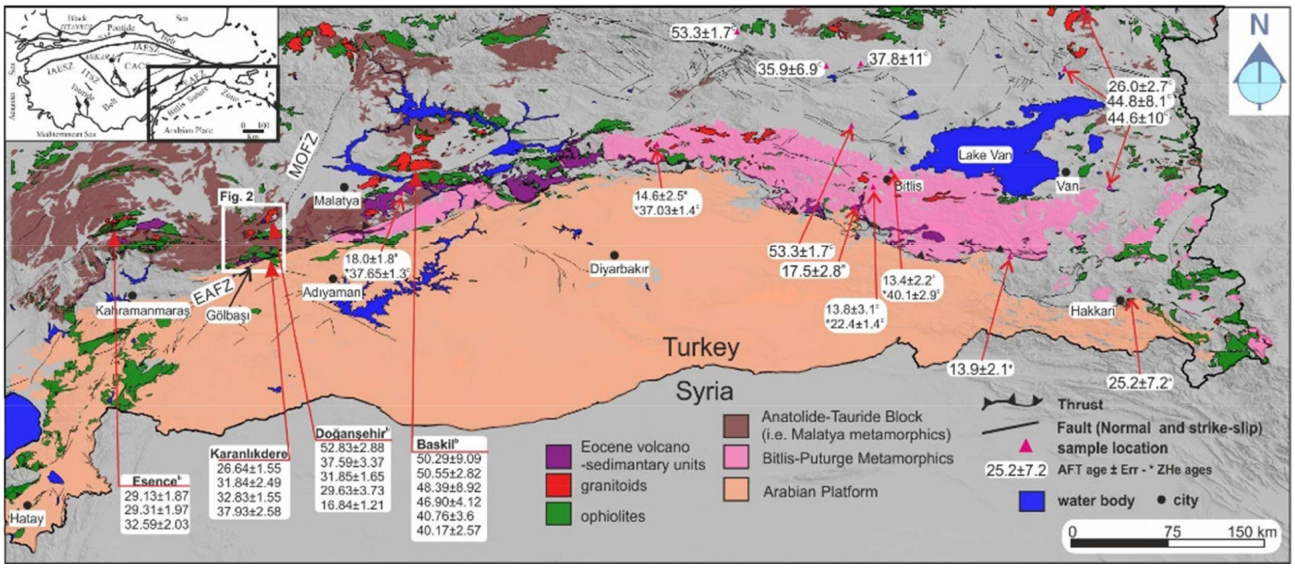

Figure 1. Generalized geological map of Southeast Anatolian Orogenic Map, SE Turkey (Yılmaz, 1993; Bozkurt and Mittwede, 2001; Bilgiç, 2002; Günay and Şenel, 2002; Şenel and Ercan, 2002; Tarhan, 2002; Ulu, 2002). Low-temperature thermochronology data from Okay et al. (2010); Karaoğlan et al. (2016); Cavazza et al. (2018) (* indicates ZHe ages). ITSZ: Inner Tauride Suture Zone; İAESZ: İzmir-Ankara-Erzincan Suture Zone; CACC: Central Anatolian Crystalline Complex; MOFZ: Malatya-Ovacık Fault Zone; EAFZ: East Anatolian Fault Zone.

Yılmaz et al., 1993; Yılmaz, 2019). The age interval of these sediments should mark the most active time interval of the imbrication. This corresponds to (i) the end of a collisional event between the Bitlis-Pütürge continental margin (latterly subduction-related metamorphic massif) in the south and a nappe zone belonging to Tauride-Anatolide plate in the north during late Cretaceous (Oberhänsli et al., 2010; Oberhänsli et al., 2012; Oberhänsli et al., 2014; Karaoğlan et al., 2016; Yılmaz, 2019), and (ii) initiation of another continental collision event in early Miocene between the subduction-related metamorphic rocks of Bitlis-Pütürge Massif in the north and the main Arabian land in the south (Robertson et al., 2012; Karaoğlan et al., 2016; Robertson et al., 2016; Açlan and Altun, 2018; Açlan and Duruk, 2018; Topuz et al., 2019; Yılmaz, 2019; Gülyüz et al., 2020).

The low-temperature thermochronology (LTT) data obtained from the region vary, based on the tectonic locations, elevations, and/or stratigraphic positions of the sampling points, between Paleocene and late Miocene showing that the different elements of the main units affected by different tectonic regimes such as collisional processes (i.e. continental or arc-continent) and/or mantle processes (i.e. delamination, slab break-off) (Okay et al., 2010; Lefebvre et al., 2015; Karaoğlan et al., 2016; Cavazza et al., 2018) (Figure 1).

Except for one, almost all LTT studies are based on individual sampling sites and scattered along the SAOB. No profile data exists for comparison and the calculation of either the uplift rate or collision rate (Figure 1). Lefebvre et al. (2015) provide apatite U-Th/He (AHe) and zircon U-Th/He (ZHe) data from an elevation profile within the Pütürge Metamorphic Complex created by Sürgü fault. They present LTT ages for that profile ranging between 30 Ma and 5 Ma, and associate the older ages with the Oligocene activation of the Sürgü Fault. Okay et al. (2010) present apatite fission track (AFT) data for the low-temperature exhumation of Bitlis-Pütürge metamorphics. Their data scattered on the unit varies between 25–18 Ma and 13 Ma. The authors proposed that their data support an early Miocene continental collision. Cavazza et al. (2018) present AFT, ZHe, and the data from Eastern Anatolia comprising the imbrication zone and Nappe zone of the SAOB. Similar to Okay et al. (2010), their data scattered along the region vary between 67 Ma and 19 Ma. The authors proposed that the older ages are related to the exhumation of Bitlis-Pütürge metamorphics, and younger ages are interpreted as the result of a continental collision event during the mid-Miocene. On the other hand, Karaoğlan et al. (2016) deal with the Esence, Doğanşehir, and Baskil granitoids outcropping in the lower nappe. They applied zircon U-Pb, amphibole, biotite, and feldspar Ar-Ar and AFT geo/thermo-chronology methods on these granitoids. Their results show that the Esence and Baskil granitoids formed during the late Cretaceous and cooled through 300 °C in 6–10 Ma. The AFT ages of the study are grouped in Eocene and Oligocene. The authors support an uplift model indicating Eocene arc setting and Oligocene

continental collision setting for the region. In addition to the LTT data directly from the SOAB, Late Eocene to Early Miocene LTT ages of Darin et al. (2018) from the Sivas Basin, Central Anatolia, the ages of Ballato et al. (2018) from the central Pontides and Albino et al. (2014) from eastern Pontides are interpreted as the response of soft collision/trench advance (late Eocene) and hard collision (early Miocene) events along the SOAB. On the other hand, the similar LTT ages of Gülyüz et al. (2019) and Gulyuz (2020) from the southern margin of the Pontides and the Central Pontides, respectively, are interpreted as the results of continental collision and the postcollisional further convergence events along the main (northern) suture zone.

LTT studies on imbricated zones of orogenic belts are good candidates to (i) constrain the timing of the initiation, and the termination of imbrication and (ii) give quantitative growth/uplift/exhumation rates of the imbrication zones. In this sense, this study focuses on the formation and the exhumation history of the Karanlıkdere granitoid located at Gölbaşı (Adıyaman) region exposed within the imbricated zone of the SAOB which allows enlighten the uplift and/or exhumation dynamics of an imbrication zone, and also the region by using low-temperature thermochronology. The lack of LTT age-elevation profiles in the region raises doubts in interpreting the geological evolution of the region. This paper provides the first age-elevation profile of the apatite fission track data from Karanlıkdere granitoid within the imbrication zone of the SAOB, to shed some light on the progressive evolution of the imbricated zone of the SAOB.

2. Geological Setting

The Karanlıkdere granitoid is exposed in the E- W directed zone of imbrication within the SAOB between Helete (Kahramanmaraş), Gölbaşı (Adıyaman), and Erkenek (Doğanşehir- Malatya). The main body of the unit outcrops at Karanlıkdere valley near the tunnels of Gölbaşı- Erkenek road in front of the Malatya metamorphics (Figures 1 and 2).

The zone of imbrication, where the Karanlıkdere granitoid is outcropped, hosts NEE/SWW-trending, northward-dipping thrust slices squeezed between the Malatya metamorphics to the north, and the Arabian platform to the south. The imbricated thrust slices include Upper Cretaceous-Lower Miocene strata, together with the Upper Cretaceous Ophiolitic rocks and metamorphic rocks, which are generally disturbed. Imbrication in the region is clearly evidenced by the older units on top of the younger units. The uppermost stack of the imbricated zone consists of Upper Cretaceous Helete volcanics, Meydan Ophiolite, and Harami formation. All of these units thrust over the Middle to Upper Eocene volcanic and volcano-clastic rocks (Savran and Alacık formations) in the region (Yıldırım and Yılmaz, 1991; Yiğitbaş and Yılmaz, 1996b; Yılmaz, 2019). Such imbrication association in the region is defined as an Eocene-Oligocene mélange (Bulgurkaya mélange) (Herece, 2008). The Eocene-Miocene units of this region were mapped as late Cretaceous Meydan Melange by Nurlu et al. (2016), but they are also defined as Eocene, Oligocene and Miocene marine units by Yıldırım and Yılmaz (1991) and Akıncı et al. (2016). The imbrication zone (melange), including Karanlıkdere granitoid, also thrust over the Lower Miocene Lice formation (flysch succession) of the Arabian platform in the region. However, this tectonic relation is not observed in the entire region, and at some places, the younger units unconformably cover the imbrication zone. Similar association is also valid for the nummulite bearing limestones and the older units of the imbrication zone (Figure 2) (Yıldırım and Yılmaz, 1991; Yiğitbaş and Yılmaz, 1996b; Herece, 2008; Yılmaz, 2019).

The northern basement is defined as Malatya metamorphics for this study. Metamorphism degree for this basement is proposed as greenschist facies (Perinçek and Kozlu, 1984; Yılmaz et al., 1992; Yılmaz et al., 1993; Hozatlıoğlu et al., 2019). The unit tectonically overlies the imbricated zone but only has reportable tectonic contact with the Harami formation and Meydan ophiolite (Figure 2, 3a). The association between turbiditic Harami formation, Meydan ophiolite, Helete volcanics, northerly located Malatya metamorphic and southerly located subduction-related metamorphics of Bitlis-Pütürge massif is explained by series of subduction, accretion, and collision events before Cenozoic (Erdoğan, 1975; Perinçek and Kozlu, 1984; Yıldırım and Yılmaz, 1991; Yılmaz, 1993, 2019).

To the south of the study area, the Cambrian to Miocene sedimentary successions of the Arabian platform are exposed, but no metamorphism sign is documented for these units, even though the older units show similar successions to the Malatya metamorphics and Bitlis-Pütürge massif (Figures 2 and 3a) (Göncüoğlu and Turhan, 1984; Yılmaz et al., 1993; Robertson et al., 2016; Yılmaz, 2019).

The Helete volcanics tectonically overlies the Meydan ophiolite (Karaoğlan et al., 2021). However, in the previous studies, the contact was reported vice versa (Yıldırım and Yılmaz, 1991; Yıldırım, 2015; Nurlu et al., 2016). The unit is cut by the dykes of Karanlıkdere granitoid at various levels ranging from a few centimeters to hundreds of meters (Yıldırım and Yılmaz, 1991; Yıldırım, 2015; Karaoğlan et al., 2021).

The Karanlıkdere granitoid; (i) intrudes into the various components of the imbrication zone such as the Meydan ophiolite, the Helete volcanics, and the Malatya

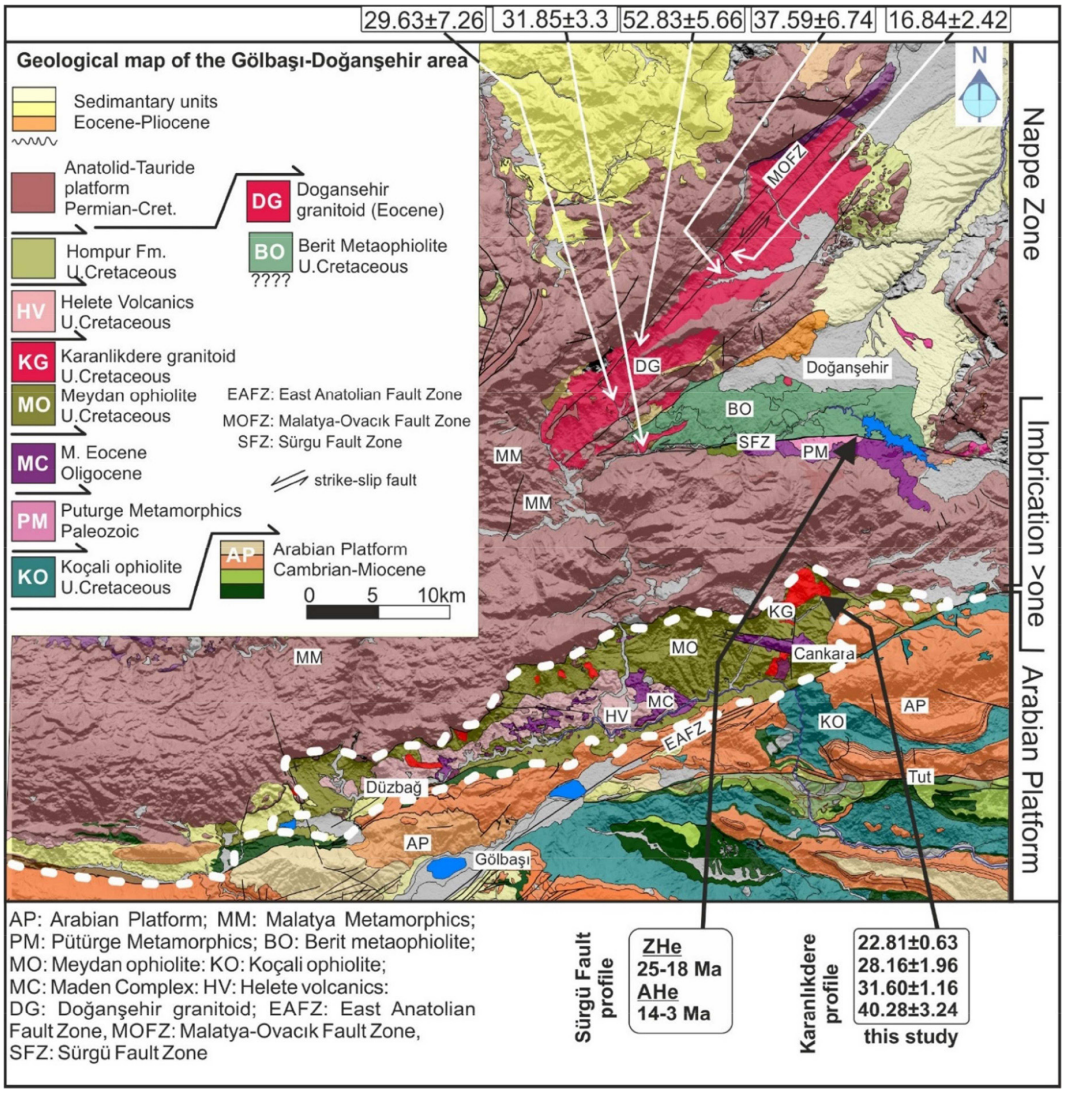

Figure 2. Geology map of the Gölbaşı (Adıyaman) and Doğanşehir (Malatya) region (modified after (Bilgiç, 2002; Ulu, 2002; Karaoğlan et al., 2013). LTT data from Lefebvre et al. (2015); Karaoğlan et al. (2016).

metamorphics (Figures 2 and 3a–3d) and (ii) took place in the deformation within the imbrication zone and exhumed to the surface temperatures along the reverse faults of the imbrication system.

3. Methodology

Five samples were taken from the relatively fresh outcrops of the Karanlıkdere granitoid regarding their altitudes to illustrate the uplift rate. The altitudes were recorded using a satellite and barometry-controlled GPS.

The samples were examined under a polarized microscope for their petrographic features using a Leica polarized microscope at 2.5X.

The mineral separation, including crushing, sieving, magnetic and heavy liquid separation, was performed at Çukurova University Geology Department (Adana, Turkey). One sample (YSF-AFT1) was selected to measure the granitoid's crystallization age. The crystallization age of the unit was measured by the LA-ICP-MS zircon U-Pb method at the Central Research Laboratories of Çukurova University.

An ESI Nd-YAG laser attached to Perkin Elmer Nexion 2000P ICP-MS was used for the U-Pb measurements. The data acquisition includes a 20 s background measurement followed by a 30 s sample ablation. The laser was used in single spot mode with 25–40 µm spot size at 6–7 J/cm2 energy with a 10 Hz repetition rate. He gas was used to carry the ablated material to the ICP-MS. The ICP-MS was used in time-resolved mode and was calibrated using the standard glass NIST SRM 612 to obtain the maximum

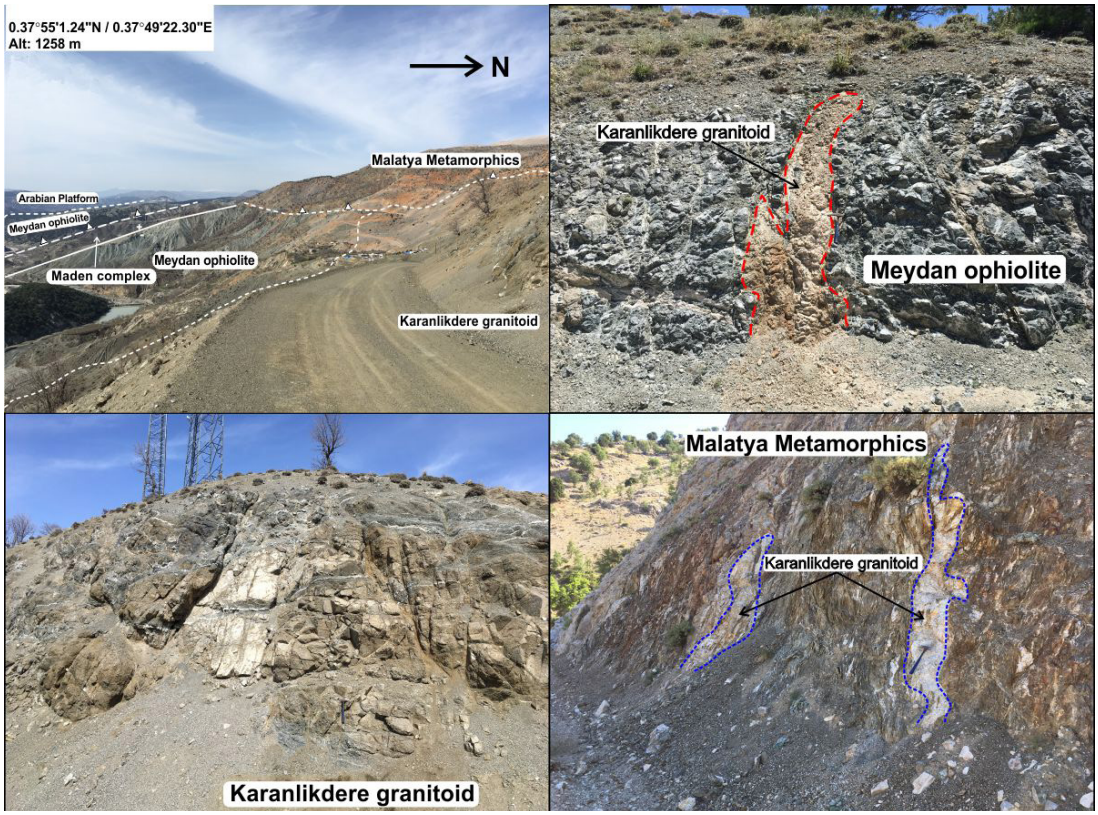

Figure 3. Field photos of the Karanlıkdere granitoid, a) general view showing the relation between the Malatya metamorphics, Meydan ophiolite, Maden mélange and the Karanlıkdere granitoid, b) general view of the Karanlıkdere granitoid, c) the schists of Malatya metamorphics cut by the Karanlıkdere granitoid, d) the gabbros of the Meydan ophiolite cut by the Karanlıkdere granitoid.

U+ signals with ThO/Th ratio <0.5%. Ar gas was used for the plasma gas, and during the analyses, 202Hg, 204Pb, 206Pb, 207Pb, 208Pb, 232Th, 235U, and 238U isotopes were measured at 10 ms, 10 ms, 40 ms, 40 ms, 10 ms, 10 ms, 10 ms, 10 ms, respectively. The GJ-1 zircon was used for the primary reference, and the Plesovice and 91500 reference zircons were used as secondary reference materials within the sample batch to test the accuracy and external reproducibility (Jackson et al., 2004; Wiedenbeck et al., 2004; Slama et al., 2008) (see supplementary file). The Iolite V4 is used for data reduction and processing (Paton et al., 2011).

Four of the five samples yielded enough apatite minerals for AFT dating. The extracted apatite minerals were mounted in epoxy resin, grinded, and polished prior to etching. The samples were etched in 5 M HNO3 for 20 s at 20 °C to reveal spontaneous tracks (Gleadow et al., 1986). The spontaneous track counts were carried out in transmitted light at a magnification of 1000X with a Nikon Eclipse microscope equipped with an XYZ motorized stage at Karfo Industrial (İstanbul, Turkey). The grain areas and track lengths were measured at the same facility.

238U measurements of the apatite grains were performed at the Central Research Laboratories of Çukurova University. The NIST 612 glass was used for calibration, and Durango (238U:12 ppm) apatite was used as a secondary reference. The LA-ICP-MS data were processed using Iolite v4 (Paton et al., 2011). Absolute age calibration was used to calculate single grain AFT ages, Hasebe et al. (2004) was used to calculate the pooled ages, whereas the IsoplotR offline version was used to calculate the central ages and dispersion (Vermeesch, 2017; Vermeesch, 2018).

The track length measurements were carried out with the same microscope at a magnification of 2000X. Three samples yielded enough confined tracks without further processes such as Cf radiation or overetching. Only the confined tracks parallel to surface and TINTs were measured.

4. Analytical results

4.1. Petrography

The petrography of the samples from Karanlıkdere granitoid shows that the unit includes granite,

microgranite, granodiorite, tonalite, diorite, microdiorite and aplitic dikes.

The samples were taken on an N-S-trending ridge near Karanlıkdere valley regarding their altitudes, without any structural units between the samples for building age-elevation profiles (Table). The samples show a high degree of alteration in the outcrops. YSF-AFT1 is a granite sample with a granular texture and comprises quartz, plagioclase, and K-feldspar as major constitute. Biotite and rare muscovite, and hornblende are mafic components, whereas zircon, apatite, sphene, and opaque minerals are observed as accessory minerals. The samples YSF-AFT2 and YSF-AFT3 are granodiorite samples showing granular, micrographic, and perthitic textures. The sample includes quartz, plagioclase, and orthoclase as major mineral phases, and biotite and rare hornblende are mafic components, whereas zircon, apatite, sphene, and opaque minerals are observed as accessory minerals. The alterations of sericitization on plagioclases and K-feldspars, epidotization, and chloritization on biotite and hornblende minerals are observed. YSF-AFT4 is a granite sample with granular and perthitic textures. The sample includes quartz, plagioclase, and K-feldspar as major constitute. Biotite and hornblende are mafic components, whereas zircon, apatite, sphene, and opaque minerals are observed as accessory minerals (Figure 4).

The CL images of the zircons U-Pb age show oscillatory zoning, indicating a magmatic origin, as well as the Th/U ratios (0.23–0.65) (Figure 5, supplementary file). The zircon U-Pb age of the sample YSF-AFT1 yields a Concordia age of 79.67 ± 0.24 Ma (Figure 6, supplementary file). The crystallization age of the Karanlıkdere granitoid is slightly younger than the Southeast Anatolian late Cretaceous granitoids such as the Esence granitoid (Kahramanmaraş)

in the west and the Baskil granitoid (Elazığ) in the east, ranging between 84 and 80 Ma (Karaoğlan et al., 2016). However, the dikes of the Karanlıkdere granitoid are dated between 92.9 ± 2.2 and 83.1 ± 1.5 Ma (Nurlu et al., 2016).

The single-grain FT ages have low dispersion and are significantly younger than the intrusion age of the granitoid (Table, Figure 7). The AFT ages range from 40.28 ± 3.4 and 22.81 ± 0.99 Ma, where the oldest AFT age is taken from the highest altitude (1483 m), and the youngest one is taken from the lowest height (1153 m) (Table, Figure 7). The chi-square test was used to check the distribution of the single-grain age populations. If the P(χ2) is >0.05, it shows that the age of the grains is composed of a single age component and the pooled age of the sample has a geological significance. On the other hand, if the P(χ2) is <0.05, the sample has multiple age components, and central age can be used to refer the sample is from different source regions or undergoes annealing caused by more than two thermal events (Table, supplementary File) (Galbraith and Laslett, 1993).

The sample YSF-AFT1 was taken from the lowest altitude at 1153m and yielded 22.81 ± 0.63 Ma pooled age. The probability of the chi-square test (P(χ2) = 0.57) for this sample indicates a homogeneous age distribution between intergrains. The track length (TL) distribution of YSF-AFT1 shows a unimodal distribution with a mean length of 12.69 μm and a standard deviation of 2.38 μm (n = 121) (Table, supplementary file).

The sample YSF-AFT2 is taken from 1216 m altitude and yields 28.16 ± 1.96 Ma pooled age. The sample passed the chi-square test indicating a homogeneous intergrain ages (P(χ2) = 1). The confined TLs show a bimodal distribution, ranging between 8 and 17 μm with a mean length of 12.80 ± 2.72 μm (Table, supplementary file).

The sample YSF-AFT3 is taken from 1386 m altitude and yields 31.6 ± 1.16 Ma pooled age. The sample passed the chi-square test indicating a homogeneous intergrain ages (P(χ2) = 0.81). The TL distribution shows a unimodal distribution with a mean length of 13.97 ± 1.61μm (Table, supplementary file).

The sample YSF-AFT4 was taken at the highest altitude of the ridge at 1483 m and yielded 40.28 ± 3.4 pooled

Table 1. The AFT data of the analyzed samples.

Sample	Lat	Long	Altitude (m)	N. Of Grains	N_s	ρ_s (10^5 cm^{-2})	^{238}U (ppm ± 2σ)	Dpar (μm)	P(χ^2)	Disp. (%)	Pooled age (Ma ± 1σ)	Central age (Ma ± 1σ)	MTL(n)
ysf-aft1	37°55'20.52" N	37° 49' 53.538" E	1153	16	2513	168	79.5 ± 44.7	2,0	0,57	2,77	22.81 ± 0.63	26.24 ± 0.59	12.69±2.38(121)
ysf-aft2	37°55'30.318" N	37° 50' 3.168" E	1216	19	432	4	6.9 ± 9.9	1,9	1,00	29,7	28.16 ± 1.96	30.5 ± 1.46	12.85±2.69(70)
ysf-aft3	37° 56'3.978" N	37°49'25.782" E	1386	43	775	54	14.96 ± 4.9	2,4	0,81	24,7	31.6 ± 1.16	32.12 ± 0.84	13.92±1.46(114)
ysf-aft4	37° 56'4.272" N	37°49' 26.208" E	1483	26	417	2	7.83 ± 1.27	1,8	0,071	27,6	40.28 ± 3.4	42.33 ± 2.63	-----
ysf-aft5	37°55'1.4704"N	37°49'22.5228"E	1260									-----	-----

Abbreviations: Ns: number of spontaneous tracks counted ;ρs: spontaneous track density; Dpar: long axis of track etch pit; MTL(n): Mean Track Length(number of lengths measured)

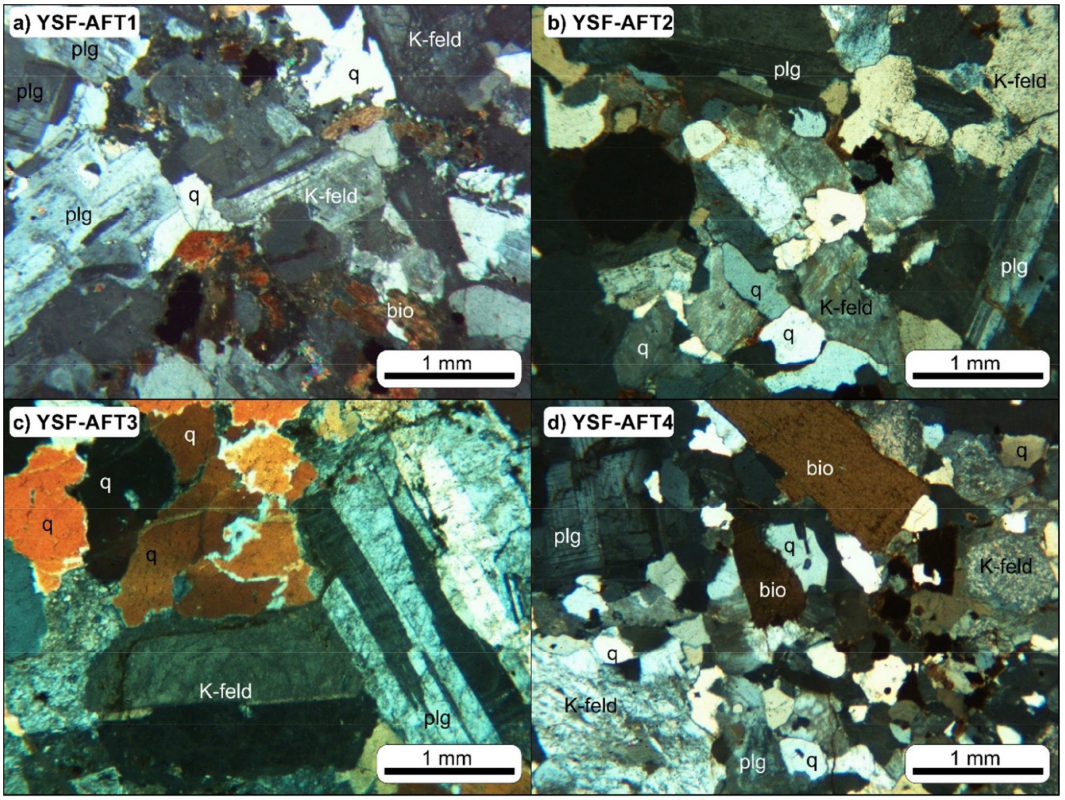

Figure 4. Thin section images of the analysed samples (q: quartz, K-feld: K-feldspar, plg: plagioclase, bio: biotite).

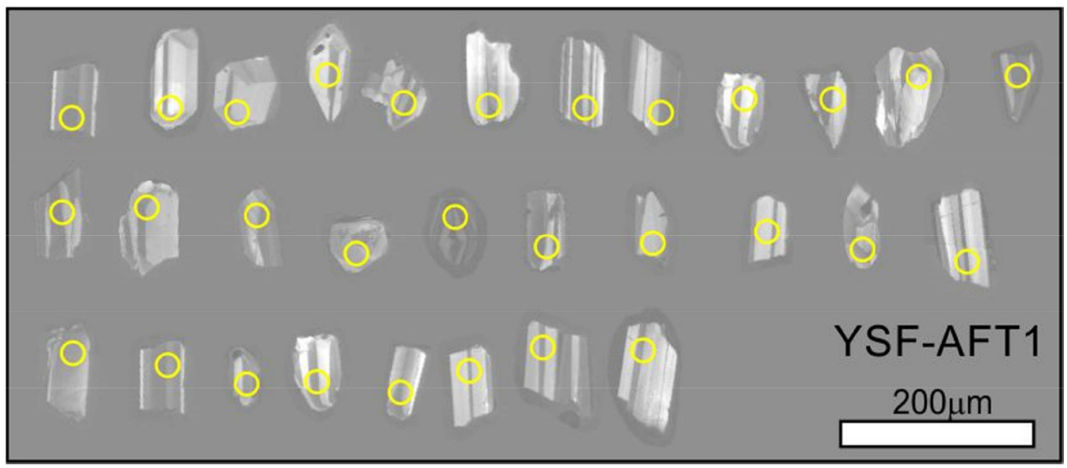

Figure 5. The CL images of the zircons extracted from sample YSF-AFT1 (yellow circles show the laser spots).

age. The sample passed the chi-square test indicating a homogeneous intergrain ages (P(χ2) = 0.07) (Table, supplementary file). This sample does not include sufficient confined tracks for meaningful statistics.

The age-elevation profile shows a direct correlation between AFT ages and their altitude (Table, Figure 7). The age-elevation profile yields an average of 0.02 ± 0.005 mm/a uplift rate indicating a slow exhumation between 40 Ma (Middle Eocene) and 22 Ma (Lower Miocene) for the late Cretaceous Karanlıkdere granitoid (Figure 7).

4.2. Thermal modeling

The HeFTy software (v1.8) was used for inverse modeling to reveal the thermal histories of the samples. The software uses track counts, confined track lengths

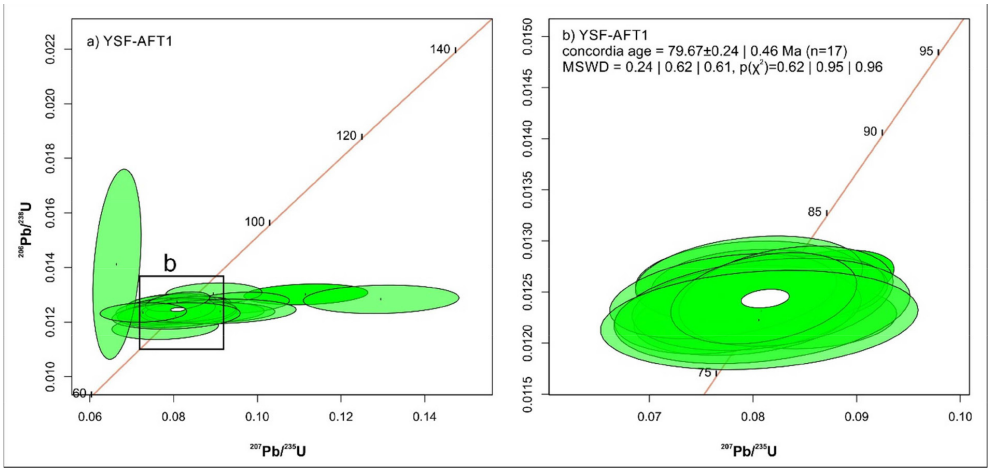

Figure 6. The Concordia diagram of the YSF-AFT1.

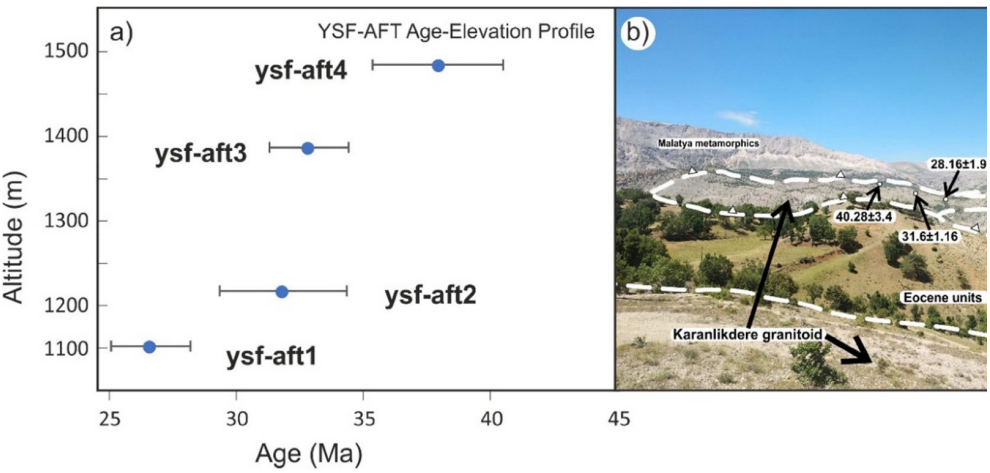

Figure 7. a) The age elevation profile of the Karanlıkdere granitoid, b) the field photo of the Karanlıkdere granitoid including AFT age data.

with c-axis angle, and Dpar values for the calculations using the annealing equation of Ketcham et al. (1999) and c-axis projection of Donelick et al. (1999). For a reliable cooling profile, at least 250 Good Paths with a minimum of 50,000 candidate temperature-time (T-t) paths were randomly generated using the Markov chain Monte Carlo algorithm for each modeling run. 79.67 ± 0.24 Ma obtained from the U-Pb dating is used for the initial constraint. YSF-AFT4 was not calculated regarding the insufficient number of track lengths to provide a statistically meaningful result.

The inverse modeling of the sample YSF-AFT1 indicates a similar age result with the measured ages (Figure 8). The sample was cooled below 120 °C after 25 Ma and remained in the PAZ until 5 Ma (Figure 8). The TL distribution implies a fast cooling rate in the PAZ after 25 Ma, which is inconsistent with the age-elevation profile and the cooling history.

The calculations indicate that the sample YSF-AFT2 was in the total annealing zone after crystallization and stayed in a flat temperature line till 20 Ma (Figure 8). The TL distribution of the sample implies that the sample remained long enough in the PAZ to shorten the old tracks, which is consistent with the slow cooling suggested by the age-elevation profile.

The sample YSF-AFT3 yields a cooling age of 30.31 ± 1.76 Ma. The T-t modeling based on track length data shows that the sample retained within the PAZ started uplifting at 35 Ma and cooled above 60 °C before 10 Ma (Figure 8).

The cooling profiles show a gradual trend of uplift above 60 °C initiated at 12-13Ma (YSF-AFT3), continued 10Ma (YSF-AFT2), and finally 5 Ma (YSF-AFT1) regarding the altitude. This uplift also indicates that the age elevation profile was not affected by any tectonic event between Middle Miocene and Upper Miocene-Pliocene (Figure 8).

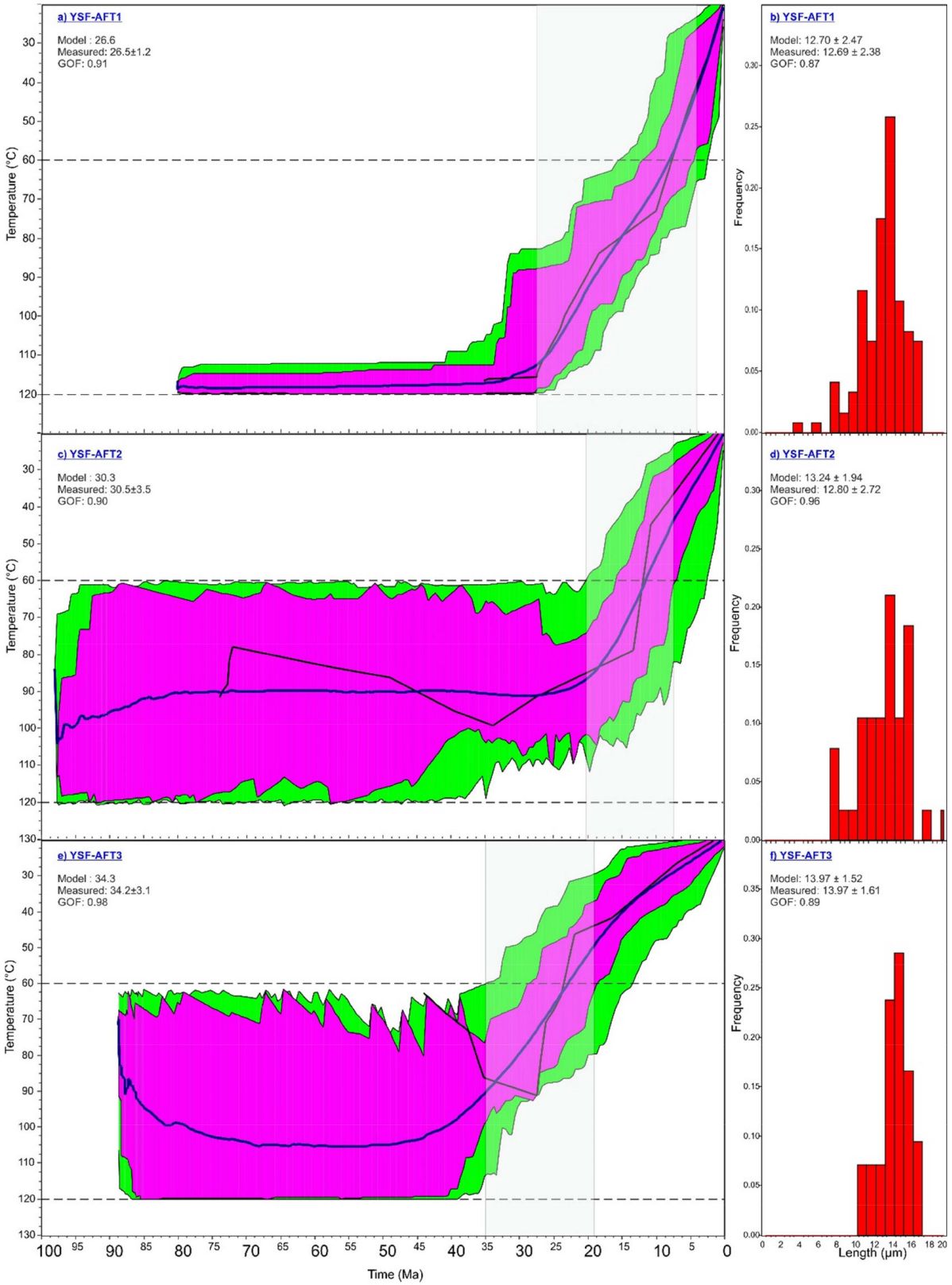

Figure 8. The inverse modeling of the samples YSF-AFT1, YSF-AFT2, and YSF-AFT3 were calculated by HeFTy (Ketcham, 2005). The black line indicates the best fit, the blue line indicates the weighted mean path, the purple area indicates good fit, and the green area indicates acceptable fit.

5. Discussion

5.1 Growth of imbrication zone along SAOB evidenced by thermal models

From four samples, three thermal models were created. Available track length measurements from the sample YSF-AFT4 were not sufficient to create a statistically consistent model. Fortunately, the rest of the samples allowed to create consistent models. According to these models, the granitoid body started to undergo relatively fast exhumation after approximately 25 Ma after stable very slow exhumation (almost flat) for the granitoid body. Such an exhumation trend for a granitoid exposure, which might be considered as a relatively deep emplaced body in an imbrication zone, can be explained by different exhumation processes. The first suggesting; (i) low deformation rate during subduction of oceanic slab or elongated continental crust (trench advance-c.f Ballato et al., 2018) of southern Neo-Tethys due to low friction rate between the overriding plate and the down-going oceanic slab and the lack of continental obstacle with low density in front of the overriding plate and latterly (ii) high deformation rate during continental collision along the SAOB, can easily explain initial (pre- approximately 25 Ma) slow and latter fast exhumation rates for the body (Figure 9). However, the geometry of thrust faults forming the imbrication stacks may also play a role in such an exhumation trend (Figure 9a). In the case of a flat or low angle decollement surface below the granitoid body during the commencement of the imbrication tectonics in the region, the body may exhume at very low rates before its arrival to steeply dipping fault surface. In the case of Karanlıkdere granitoid, the body may have exhumed at very low rates up to approximately 25 Ma and continued with high rates due to changes in the dip of the fault plane (Figure 9b). Simply, both processes might explain the exhumation trend of the Karanlıkdere granitoid. The first process (with trench advance setting) and the second processes fit with the interpretations of Ballato et al. (2018) and Darin et al. (2018) suggesting initial soft and subsequent hard collision model; however, the existence of early Miocene arc-related granitoid in the Eastern Anatolia at the north of promontory thrust of the SAOB does not support preearly Miocene collision model (Açlan and Altun, 2018; Açlan and Duruk, 2018; Oyan, 2018). In this regard, here it is suggested that initially, the granitoid body exhumed with very low rates within an imbrication zone at the southernmost margin of the overriding Anatolide-Tauride plate during oceanic slab subduction, and latterly it started to exhume with high rates due to continental collision event. Also, the low and high exhumation trends for the granitoid body were enhanced by the geometry of a thrust fault acting as an arc-shaped conveyor by lying below the granitoid (Figures 9a and 9b).

5.2. Regional implications

The zone of imbrication of the SAOB formed between the passive Arabian platform to the south and the Tauride active margin to the north, as a result of the amalgamation of the continental and oceanic fragments during the late Cretaceous-Miocene. The imbrication zone comprises trust sheets of ophiolites, mélange, granitoid bodies, volcanic arc units as well as sedimentary and volcanic units formed within this unit (Perinçek and Kozlu, 1984; Yılmaz, 1993; Yiğitbaş and Yılmaz, 1996a, b; Yılmaz and Gürer, 1996; Robertson et al., 2006; Robertson et al., 2012; Yılmaz, 2019).

The LTT data obtained from the SAOB accumulating day by day. However, the available LTT data are still restricted, the results indicate that the exhumation/uplifting across the suture zone initiated since late Cretaceous-early Paleogene and continued until the late Miocene (Oberhänsli et al., 2010; Okay et al., 2010; Oberhänsli et al., 2012; Albino et al., 2013; Oberhänsli et al., 2014; Lefebvre et al., 2015; Karaoğlan et al., 2016; Cavazza et al., 2018; Yılmaz, 2019).

The collisional processes between the Anatolide-Tauride Block and the Arabian platform are still under debate among scientists. The proposed timing of the collision according to geochemistry, magmatism, metamorphism, stratigraphy, sedimentation and field relations as well as thermochronology data; ranges from late Cretaceous to Upper-Middle Miocene (Hall, 1976; Şengör and Yılmaz, 1981; Yılmaz, 1993; Allen and Armstrong, 2008; Oberhänsli et al., 2010; Okay et al., 2010; Oberhänsli et al., 2012; Robertson et al., 2012; Oberhänsli et al., 2014; Schildgen et al., 2014; Karaoğlan et al., 2016; Duman et al., 2017; Sar et al., 2019; Yılmaz, 2019; Gülyüz et al., 2020).

Recent studies depict the existence of two oceans between Tauride-Anatolide and Arabian platform, where Bitlis-Pütürge metamorphic complex was in between these two oceans during the late Cretaceous. The Bitlis-Pütürge metamorphics collided Tauride-Anatolide platform during the late Cretaceous following the demise of the Berit ocean in a north-dipping subduction. The Bitlis-Pütürge metamorphics underwent a blueschist metamorphism during this continental collision (Oberhänsli et al., 2010; Oberhänsli et al., 2012; Robertson et al., 2012; Oberhänsli et al., 2014; Karaoğlan et al., 2016; Yılmaz, 2019). The main branch of the southern Neo-Tethys survived until the early Miocene and the oceanic or continental fragments imbricated in front of the Tauride active margin forming the zone of imbrication since the late Cretaceous (Yılmaz, 2019). The current exposures of the Meydan ophiolite and the Karanlıkdere granitoid indicate that they have not experienced either the subduction beneath the Malatya metamorphics nor obduction on to Pütürge metamorphics

or later nappe movements. This results in (i) undistribution on the LTT data of the granitoid and (ii) consistent AFT age results and thermal models indicating steady uplift of the Karanlıkdere granitoid along an elevation profile, in contrast to the Baskil, Esence and Doğanşehir granitoids cropping out within the nappe zone (Karaoğlan et al., 2016) (Figure 10).

The LTT data obtained from the Bitlis-Pütürge metamorphics and the Nappe zone of the SAOB range between early Paleocene and latest Miocene including ZHe, AFT and AHe data (Okay et al., 2010; Lefebvre et al., 2015; Karaoğlan et al., 2016; Cavazza et al., 2018). The older ages are associated with the closure of the Berit Ocean and the continental collision between the Bitlis-

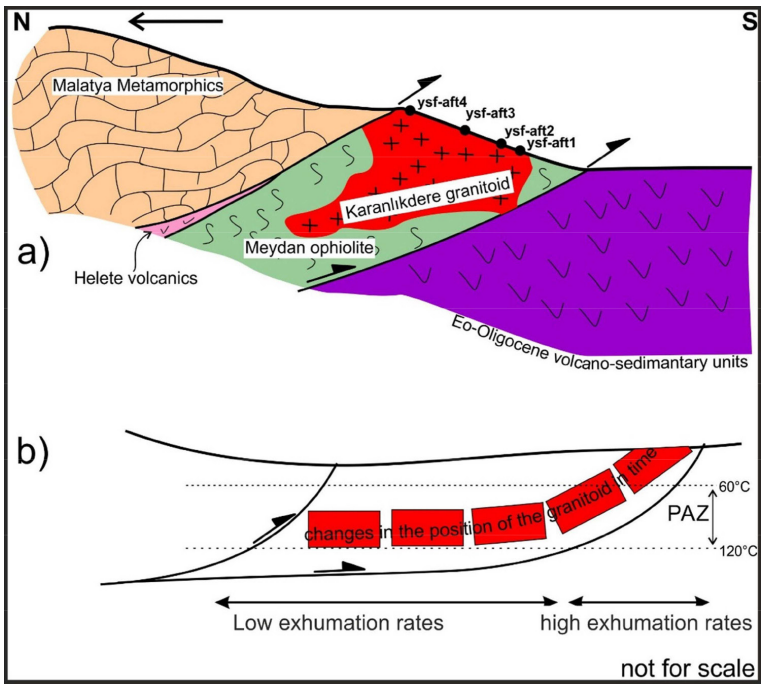

Figure 9. Cross section illustrating the trusting within the imbrication zone and sample locations, b) conceptual model explaining possible low and high exhumation rates in an imbrication zone. See text for the details.

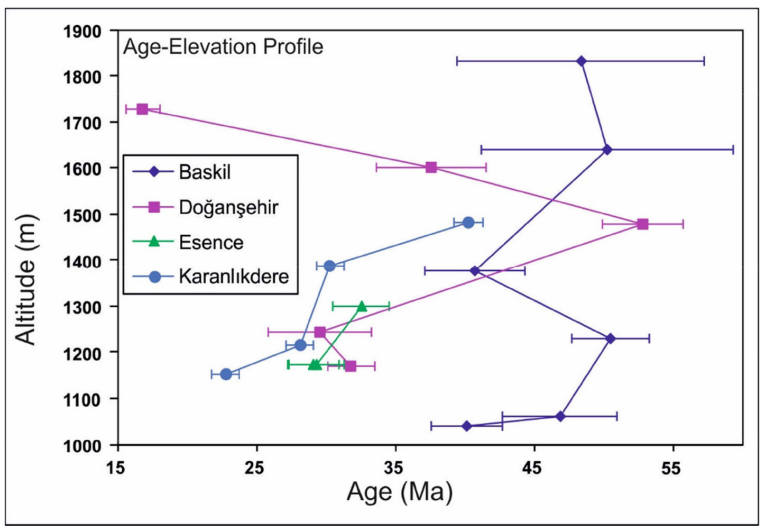

Figure 10. The AFT age-elevation profiles of the granitoids outcropped along the SAOB. Data from Karaoğlan et al. (2016) and this study.

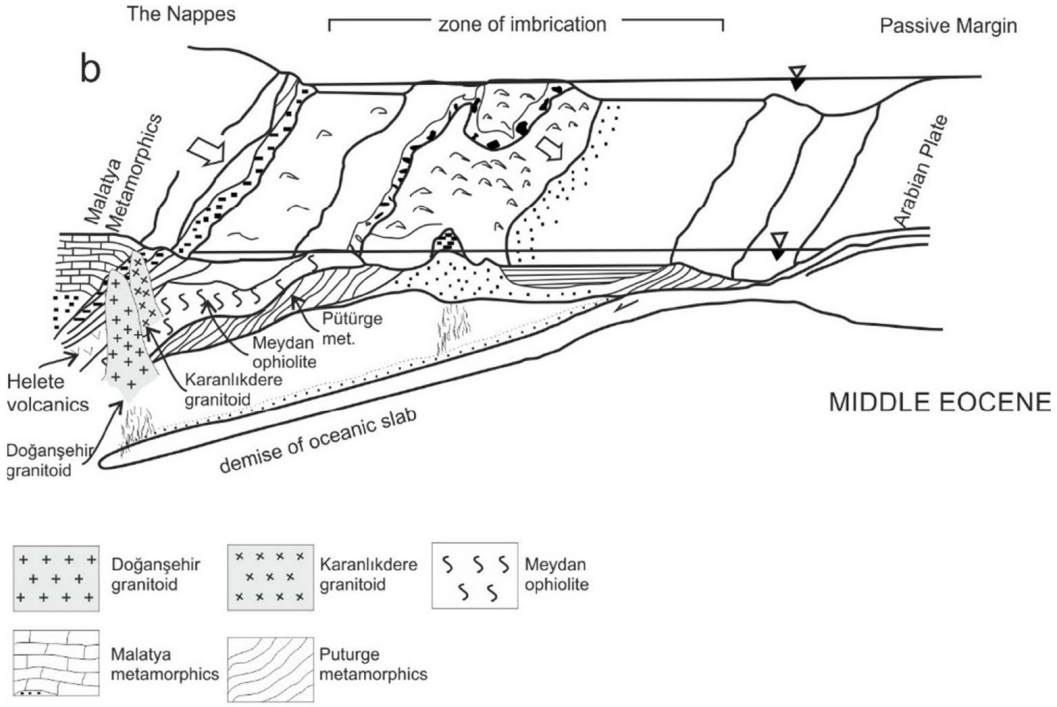

Figure 11. The middle Eocene tectonic setting of the Southeast Anatolian Orogenic Belt (adapted from Yılmaz (1993)).

Pütürge metamorphics and Tauride Block. During Eocene, arc magmatism developed in the nappe zone and intruded into nappes (i.e. Malatya metamorphics) (Karaoğlan et al., 2013). This arc setting let the region uplift during Eocene within the nappe zone (Karaoğlan et al., 2016) (Figure 11). In front of the nappes, the north-dipping subduction accreted the nappe piles continuously without any interruption during middle-late Eocene to early Miocene (Figure 11). The early Miocene witnesses the final continental collision between the Tauride Block to the north and the Arabian platform to the south as evidenced by low-temperature thermochronology, stratigraphy, paleomagnetism, and magmatism (Keskin, 2003; Okay et al., 2010; Cavazza et al., 2018; Yılmaz, 2019; Gülyüz et al., 2020; Robertson et al., 2021). Briefly, the thermal models presented here are consistent with the early Miocene continental collision scenario by indicating very low uplift rates during Eocene-Oligocene time interval and the initiation of fast uplift rates in the early Miocene.

6. Conclusion

LA-ICP-MS zircon U-Pb and apatite fission track thermochronology were applied to samples collected from the Karanlıkdere granitoid within the imbrication zone of the Southeast Anatolian Orogenic Belt. The samples were collected on a ridge without any tectonic structure to illustrate the age-elevation profile for the AFT data. The results indicate that:

- The Karanlıkdere granitoid formed during the late Cretaceous (79–80 Ma), similar to Esence granitoid (Kahramanmaraş) to the west, and Baskil Granitoid (Elazığ) to the east which are outcropped in the nappe zone.
- The Karanlıkdere granitoid intruded into late Cretaceous Meydan ophiolite, late Cretaceous Helete volcanics and overriding Malatya metamorphics indicating that these units were juxtaposed prior to magmatism.
- The age-elevation profiles obtained from the apatite fission track data show that the Karanlıkdere granitoid uplifted without any interruption during the middle-late Eocene to the early Miocene.
- The results indicate that the growth of the imbrication zone in front of the nappes of the SAOB continued in a steady-state mode with a slow uplift rate of 0.02 ± 0.005 mm/a between middle-late Eocene and early Miocene, which is also confirmed by the thermal models.
- The cooling profiles confirm the age-elevation profile as well as the increase in the cooling rates during the early-middle Miocene, which might be explained by continental collision during this period.

Acknowledgement

This work was financially supported by the Research Fund of the Adıyaman University (Project no: TEBMYOMAP/2019-0001). I would like to thank Dr. Fatih Karaoğlan for performing AFT and zircon U-Pb analyses.

References

Açlan M, Altun Y (2018). Syn-collisional I-type Esenköy Pluton (Eastern Anatolia-Turkey): An indication for collision between Arabian and Eurasian plates. Journal of African Earth Sciences 142: 1-11.

Açlan M, Duruk Hİ (2018). Geochemistry, zircon U-Pb geochronology, and tectonic setting of the Taşlıçay Granitoids, Eastern Anatolia, Turkey. Arabian Journal of Geosciences 11: 336.

Akıncı AC, Robertson AHF, Ünlügenç UC (2016). Late Cretaceous–Cenozoic subduction–collision history of the Southern Neotethys: new evidence from the Çağlayancerit area, SE Turkey. International Journal Earth Science 105: 315-337.

Albino I, Cavazza W, Zattin M, Okay AI, Adamia S et al. (2013). Far-field tectonic effects of the Arabia–Eurasia collision and the inception of the North Anatolian Fault system. Geological Magazine 151: 372-379.

Albino I, Cavazza W, Zattin M, Okay AI, Adamia S et al. N (2014). Far-field tectonic effects of the Arabia-Eurasia collision and the inception of the North Anatolian Fault system. Geological Magazine 151: 372-379.

Allen MB, Armstrong HA (2008). Arabia-Eurasia collision and the forcing of mid-Cenozoic global cooling. Palaeogeography, Palaeoclimatology, Palaeoecology 265: 52-58.

Ballato P, Parra M, Schildgen TF, Dunkl I, Yıldırım C et al. (2018). Multiple Exhumation Phases in the Central Pontides (N Turkey): New Temporal Constraints on Major Geodynamic Changes Associated With the Closure of the Neo-Tethys Ocean. Tectonics 37: 1831-1857.

Bilgiç T, (2002). 1:500000 ölçekli Sivas paftası Jeoloji Haritası No:10, in: Şenel, M (Ed.). MTA, Ankara, Türkiye.

Bozkurt E, Mittwede SK (2001). Introduction to the Geology of Turkey—A Synthesis. International Geology Review 43: 578-594.

Cavazza W, Cattò S, Zattin M, Okay AI, Reiners P (2018). Thermochronology of the Miocene Arabia-Eurasia collision zone of southeastern Turkey. Geosphere 14: 2277-2293.

Darin MH, Umhoefer PJ, Thomson SN (2018). Rapid Late Eocene Exhumation of the Sivas Basin (Central Anatolia) Driven by Initial Arabia-Eurasia Collision. Tectonics 37: 3805-3833.

Donelick RA, Ketcham RA, Carlson WD (1999). Variability of apatite fission-track annealing kinetics: II. Crystallographic orientation effects. American Mineralogist 84: 1224-1234.

Duman TY, Robertson AHF, Elmacı H, Kara M (2017). Palaeozoic-Recent geological development and uplift of the Amanos Mountains (S Turkey) in the critically located northwesternmost corner of the Arabian continent. Geodinamica Acta 29: 103-138.

Erdoğan T (1975). Gölbaşı civarının jeolojisi: TPAO Arama Grubu, Rapor no.929, 17s., Ankara.

Galbraith RF, Laslett GM (1993). Statistical-Models for Mixed Fission-Track Ages. Nuclear Tracks and Radiation Measurements 21: 459-470.

Gleadow AJW, Duddy IR, Green PF, Lovering JF (1986). Confined fission track lengths in apatite: a diagnostic tool for thermal history analysis. Contributions to Mineralogy and Petrology 94: 405-415.

Göncüoğlu C, Turhan N (1984). Geology of the Bitlis Metamorphic Belt, In: Tekeli, O, Göncüoğlu, MC editors. Geology of The Taurus Belt. Mineral Research and Expolaration Instutute of Turkey (MTA), Ankara, pp. 237-244.

Göncüoğlu MC (2019). A Review of the Geology and Geodynamic Evolution of Tectonic Terranes in Turkey, In: Pirajno, F, Ünlü, T, Dönmez, C, Şahin, MB editors. Mineral Resources of Turkey. Springer International Publishing, Cham, pp. 19-72.

Görür N, Oktay FY, Seymen İ, Şengör AMC (1984). Palaeotectonic evolution of the Tuzgölü basin complex, Central Turkey: sedimentary record of a Neo-Tethyan closure, In: DIXON, JE, ROBERTSON, AHF editors. The Geological Evolution of the Eastern Mediterranean. Geological Society Special Publications, London, pp. 467-482.

Görür N, Tüysüz O, Celal Şengör AM (1998). Tectonic Evolution of the Central Anatolian Basins. International Geology Review 40: 831-850.

Gulyuz E (2020). Apatite fission track dating of the Beypazari Granitoid: insight for the inception of collision along the Northern Neotethys, Turkey. Geodinamica Acta 32: 1-10.

Gülyüz E, Durak H, Özkaptan M, Krijgsman W (2020). Paleomagnetic constraints on the early Miocene closure of the southern Neo-Tethys (Van region; East Anatolia): Inferences for the timing of Eurasia-Arabia collision. Global and Planetary Change 185: 103089.

Gülyüz E, Özkaptan M, Kaymakci N, Persano C, Stuart FM (2019). Kinematic and thermal evolution of the Haymana Basin, a fore-arc to foreland basin in Central Anatolia (Turkey). Tectonophysics.

Günay Y, Şenel M, (2002). Turkey Geological Map, Sheet Cizre: Ankara, Turkey: Maden Tetkik ve Arama Genel Müdürlüğü, scale 1:500,000.

Hall R (1976). Ophiolite emplacement and the evolution of the Taurus suture zone, southeastern Turkey. Geological Society of America Bulletin 87: 1078-1088.

Hasebe N, Barbarand J, Jarvis K, Carter A, Hurford AJ (2004). Apatite fission-track chronometry using laser ablation ICP-MS. Chemical Geology 207: 135-145.

Herece E, (2008). Doğu Anadolu Fayı (DAF) Atlası. General Directorate of Mineral Research and Exploration (MTA), Ankara, Türkiye.

Hinsbergen DJJ, Maffione M, Plunder A, Kaymakcı N, Ganerød M et al. (2016). Tectonic evolution and paleogeography of the Kırşehir Block and the Central Anatolian Ophiolites, Turkey. Tectonics 35: 983-1014.

Hozatlıoğlu D, Bozkaya Ö, Yalçın H, Yılmaz H (2019). Göksun, Afşin Ve Ekinözü (Kahramanmaraş) Bölgesinde Yüzeylenen Metamorfik Masiflerin Mineralojik Karakteristikleri. Bulletin of The Mineral Research and Exploration: 1-10.

Jackson SE, Pearson NJ, Griffin WL, Belousova EA (2004). The application of laser ablation-inductively coupled plasma-mass spectrometry to in situ U–Pb zircon geochronology. Chemical Geology 211: 47-69.

Karaoğlan F, Parlak O, Hejl E, Neubauer F, Klötzli U (2016). The temporal evolution of the active margin along the Southeast Anatolian Orogenic Belt (SE Turkey): Evidence from U–Pb, Ar–Ar and fission track chronology. Gondwana Research 33: 190-208.

Karaoğlan F, Parlak O, Robertson A, Thöni M, Klötzli U et al. (2013). Evidence of Eocene high-temperature/high-pressure metamorphism of ophiolitic rocks and granitoid intrusion related to Neotethyan subduction processes (Doğanşehir area, SE Anatolia), In: Robertson, AHF, Parlak, O, Ünlügenç, UC editors. Geological Development of Anatolia and the Easternmost Mediterranean Region. Geological Society, London, Special Publications, London, pp. 249-272.

Karaoğlan F, Yıldırım N, Yıldırım E, Topak Y (2021). The Geology of Gölbaşı (Adıyaman) Region: The Upper Cretaceous -Eocene Evolution of the Southeast Anatolian Orogenic Belt. 73th Geological Congress of Turkey, pp. 453-454.

Keskin M (2003). Magma generation by slab steepening and breakoff beneath a subduction-accretion complex: An alternative model for collision-related volcanism in Eastern Anatolia, Turkey. Geophysical Research Letters 30: n/a-n/a.

Ketcham RA (2005). Forward and Inverse Modeling of Low-Temperature Thermochronometry Data, In: Reiners, PW, Ehlers, TA editors. Low-Temperature Thermochronology: Techniques, Interpretations, and Applications. Mineralogical Society of America, pp. 275-314.

Ketcham RA, Donelick RA, Carlson WD (1999). Variability of apatite fission-track annealing kinetics: III. Extrapolation to geological time scales. American Mineralogist 84: 1235-1255.

Lefebvre C, Thomson SN, Reiners PW, Whitney DL, Teyssier C (2015). Thermochronologic evaluation of the Arabia-Anatolia collision: new results from Apatite (U-Th) He and Fission Track. EGU2015, pp. EGU2015-7623.

Nurlu N, Parlak O, Robertson A, von Quadt A (2016). Implications of Late Cretaceous U-Pb zircon ages of granitic intrusions cutting ophiolitic and volcanogenic rocks for the assembly of the Tauride allochthon in SE Anatolia (Helete area, KahramanmaraAY Region, SE Turkey). International Journal of Earth Sciences 105: 283-314.

Oberhänsli R, Bousquet R, Candan O, Okay A (2012). Dating Subduction Events in East Anatolia, Turkey. Turkish Journal of Earth Sciences 21: 1-17.

Oberhänsli R, Candan O, Bousquet R, Rimmele G, Okay A et al. (2010). Alpine high pressure evolution of the eastern Bitlis complex, SE Turkey, In: Sosson, M, Kaymakci, N, Stephenson, RA, Bergerat, F, Starostenko, V editors. Sedimentary Basin Tectonics from the Black Sea and Caucasus to the Arabian Platform. Geological Society, London, Special Publications, London, pp. 461-483.

Oberhänsli R, Koralay E, Candan O, Pourteau A, Bousquet R (2014). Late Cretaceous eclogitic high-pressure relics in the Bitlis Massif. Geodinamica Acta 26: 175-190.

Okay AI, Tüysüz O (1999). Tethyan sutures of northern Turkey, In: Durand, B, Jolivet, FL, Horváth, F editors. The Mediterranean Basins: Tertiary Extension within the Alpine Orogen. Geological Society, London, Special Publications, pp. 475-515.

Okay AI, Zattin M, Cavazza W (2010). Apatite fission-track data for the Miocene Arabia-Eurasia collision. Geology 38: 35-38.

Oyan V (2018). Ar-Ar dating and petrogenesis of the Early Miocene Taskapi-Mecitli (Ercis-Van) granitoid, Eastern Anatolia Collisional Zone, Turkey. Journal of Asian Earth Sciences 158: 210-226.

Paton C, Hellstrom J, Paul B, Woodhead J, Hergt J (2011). Iolite: Freeware for the visualisation and processing of mass spectrometric data. Journal of Analytical Atomic Spectrometry 26: 2508-2518.

Perinçek D, Kozlu H (1984). Stratigraphy and structural relations of the units in the Afşin-Elbistan-Doganşehir region (Eastern Taurus), In: Tekeli, O, Göncüoğlu, MC editors. Geology Of The Taurus Belt. Mineral Research and Expolaration Instutute of Turkey (MTA), Ankara, pp. 181-198.

Robertson A, Parlak O, Ustaömer T, Tasli K, Dumitrica P (2021). Late Palaeozoic-Neogene sedimentary and tectonic development of the Tauride continent and adjacent Tethyan ocean basins in eastern Turkey: New data and integrated interpretation. Journal of Asian Earth Science. doi: 10.1016/j.jseaes.2021.104859

Robertson A, Boulton SJ, Taslı K, Yıldırım N, İnan N et al. (2016). Late Cretaceous–Miocene sedimentary development of the Arabian continental margin in SE Turkey (Adıyaman region): Implications for regional palaeogeography and the closure history of Southern Neotethys. Journal of Asian Earth Sciences 115: 571-616.

Robertson AHF, Parlak O, Ustaomer T (2012). Overview of the Palaeozoic-neogene evolution of neotethys in the Eastern Mediterranean region (Southern Turkey, Cyprus, Syria). Petroleum Geoscience 18: 381-404.

Robertson AHF, Ustaömer T, Parlak O, Ünlügenç UC, Taslı K et al. (2006). The Berit transect of the Tauride thrust belt, S Turkey: Late Cretaceous-Early Cenozoic accretionary/collisional processes related to closure of the Southern Neotethys. Journal of Asian Earth Sciences 27: 108-145.

Sar A, Ertürk MA, Rizeli ME (2019). Genesis of Late Cretaceous intra-oceanic arc intrusions in the Pertek area of Tunceli Province, eastern Turkey, and implications for the geodynamic evolution of the southern Neo-Tethys: Results of zircon U–Pb geochronology and geochemical and Sr–Nd isotopic analyses. Lithos 350-351: 105263.

Schildgen TF, Yildirim C, Cosentino D, Strecker MR (2014). Linking slab break-off, Hellenic trench retreat, and uplift of the Central and Eastern Anatolian plateaus. Earth-Science Reviews 128: 147-168.

Şenel M, Ercan T, (2002). Turkey Geological Map, Sheet Van: Ankara, Turkey, Maden Tetkik ve Arama Genel Müdürlüğü, scale 1:500,000. Maden Tetkik ve Arama Genel Müdürlüğü, Ankara.

Şengör AMC, Yılmaz Y (1981). Tethyan Evolution of Turkey-a Plate Tectonic Approach. Tectonophysics 75: 181-241.

Slama J, Kosler J, Condon DJ, Crowley JL, Gerdes A et al. (2008). Plesovice zircon-A new natural reference material for U-Pb and Hf isotopic microanalysis. Chemical Geology 249: 1-35.

Tarhan N, (2002). 1:500000 Ölçekli Erzurum Paftası Jeoloji Haritası. No:11, in: Şenel, M (Ed.). MTA, Ankara, Türkiye.

Topuz G, Candan O, Zack T, Chen F, Li Q-L (2019). Origin and significance of Early Miocene high-potassium I-type granite plutonism in the East Anatolian plateau (the Taşlıçay intrusion). Lithos: 105210.

Ulu U, (2002). 1:500000 Ölçekli Hatay Paftası Jeoloji Haritası. No: 16, in: Şenel, M (Ed.). MTA, Ankara, Türkiye.

Ural M, Arslan M, Göncüoglu MC, Tekin KU, Kürüm S (2015). Late Cretaceous arc and back-arc formation within the Southern Neotethys: whole-rock, trace element and Sr-Nd-Pb isotopic data from basaltic rocks of the Yüksekova Complex (Malatya-Elazığ, SE Turkey). Ofioliti 40.

Vermeesch P (2017). Statistics for LA-ICP-MS based fission track dating. Chemical Geology 456: 19-27.

Vermeesch P (2018). IsoplotR: A free and open toolbox for geochronology. Geoscience Frontiers 9: 1479-1493.

Wiedenbeck M, Hanchar JM, Peck WH, Sylvester P, Valley J et al. (2004). Further characterisation of the 91500 zircon crystal. Geostandards and Geoanalytical Research 28: 9-39.

Yiğitbaş E, Yılmaz Y (1996a). Post-Late Cretaceous Strike-Slip Tectonics and Its Implications for the Southeast Anatolian Orogen, Turkey. International Geology Review 38: 818-831.

Yiğitbaş E, Yılmaz Y (1996b). New evidence and solution to the Maden complex controversy of the Southeast Anatolian orogenic belt (Turkey). Geologische Rundschau 85: 250-263.

Yıldırım E (2015). Geochemistry, petrography and tectonic significance of the ophiolitic rocks, felsic intrusions and Eocene volcanic rocks of an imbrication zone (Helete area, Southeast Turkey). Journal of African Earth Sciences 107: 89-107.

Yıldırım M, Yılmaz Y (1991). Güneydoğu Anadolu orojenik kuşağının ekaylı zonu [Imbrication zone of Southeastern Anatolian Orogenic Belt]. Türkiye Petrol Jeologları Derneği Bülteni, 3: 57-73.

Yılmaz Y (1993). New Evidence and Model on the Evolution of the Southeast Anatolian Orogen. Geological Society of America Bulletin 105: 251-271.

Yılmaz Y (2019). Southeast Anatolian Orogenic Belt revisited (geology and evolution). Canadian Journal of Earth Sciences 56: 1163-1180.

Yılmaz Y, Gürer ÖF (1996). Andırım (Kahramanmaraş) Dolayında Misis-Andırın Kuşağının Jeolojisi ve Evrimi. Turkish Journal of Earth Sciences 5: 39-55.

Yılmaz Y, Yiğitbaş E, Genç ŞC (1993). Ophiolitic and Metamorphic Assemblages of Southeast Anatolia and Their Significance in the Geological Evolution of the Orogenic Belt. Tectonics 12: 1280-1297.

Yılmaz Y, Yiğitbaş E, Yıldırım M, Genç ŞC (1992). Güneydoğu Anadolu Metamorfik Masiflerinin Kökeni. Türkiye 9. Petrol kongresi.

	Tracks	Area (μm^2)	Track Density (tracks/cm2)	U238 (ppm)	2SE(int)	Age	1SE(int)		
Grain 1	133	99614	133515	8,96	0,44	28,71	2,86		
Grain 2	61	40185	151798	8,51	0,43	34,35	4,73		
Grain 3	98	87438	112079	8,71	0,45	24,8	2,81		
Grain 4	82	53882	152184	10,17	0,47	28,83	3,45		
Grain 5	67	46349	144555	8,80	0,45	31,64	4,19		
Grain 6	72	53415	134794	8,72	0,49	29,78	3,89		
Grain 7	69	54549	126492	8,03	0,49	30,35	4,1		
Grain 8	43	29660	178692	8,94	0,46	31,24	5,03		
Grain 9	89	70466	126302	8,99	0,45	27,07	3,17		
Grain 10	98	65925	148654	9,41	0,49	30,43	3,46		
Grain 11	87	49551	175577	8,81	0,44	38,37	4,54		
Grain 12	110	94049	87189	8,83	0,44	25,53	2,75		
Grain 13	67	52909	126633	10,07	0,52	24,24	3,21		
Grain 14	72	56521	127386	9,77	0,52	25,13	3,25		
Grain 15	25	17747	101426	8,85	0,52	22,09	5,37		
Grain 16	111	78406	141571	8,58	0,40	31,78	3,36		
Grain 17	72	58344	106266	8,75	0,41	27,18	3,45		
Grain 18	99	59163	167334	10,76	0,52	29,96	3,34		
Grain 19	50	34668	144225	8,80	0,42	31,57	4,71		
Grain 20	52	42027	123730	8,76	0,45	27,22	4,02		
	1557	1144868			**Central Age**	**29,12**	**0,81**	**MSWD**	**1**
					Pooled age	**28,27**	**1,61**	**p(x2)**	**0,63**
								Disp	**0,0081**

YSF-AFT1	Track	Area (μm^2)	Density (tracks/cm2)	Average DPar(µmm)	DPar Std Deviation	U238 (ppm)	2SE(int)	Age	1SE(int)		
Grain 1	185	14356	1288660	2,2	0,0	83,44	2,60	29,75	2,22		
Grain 2	82	11133	934160	2,6	0,5	52,30	1,65	27,14	3,01		
Grain 3	296	17178	1437886	1,7	0,3	136,66	5,32	24,3	1,55		
Grain 4	72	7950	1232704	1,9	0,6	65,19	2,64	26,77	3,17		
Grain 5	137	17687	774580	1,6	0,5	62,47	2,10	23,9	2,06		
Grain 6	91	9911	918172	2,2	0,1	69,48	2,27	25,47	2,69		
Grain 7	38	8996	344598	2,1	0,6	31,14	1,03	26,14	4,24		
Grain 8	68	4441	1666291	2,3	0,2	108,68	4,85	27,15	3,36		
Grain 9	301	12492	1593020	2,3	0,2	181,08	8,18	25,64	1,81		
Grain 10	136	39976	457775	2,2	0,1	23,44	0,85	27,97	2,4		
Grain 11	264	23046	1076109	1,9	0,2	97,15	3,57	22,73	1,46		
Grain 12	141	14413	1304378	1,7	0,2	69,77	2,62	27,02	2,3		
Grain 13	315	22026	1430128	1,9	0,1	100,28	3,53	27,48	1,62		
Grain 14	182	9596	1490204	1,7	0,5	132,06	5,53	27,67	2,19		
Grain 15	101	35585	283827	2,1	0,4	21,11	0,79	25,91	2,58		
Grain 16	104	18164	572561	2,0	0,4	38,34	1,72	28,77	2,83		
	2513	266950	16805052	2,0			**Central Age**	**26,21**	**0,58**	**MSWD**	**0,9**
							Pooled Age	**22,81**	**0,99**	**p(x2)**	**0,57**
										Disp	**2,77**

YSF-AFT2		Track	Area (μm^2)	Density (tracks/cm2)	Average DPar(µmm)	DPar Std Deviation	U238 (ppm)	2SE(int)	Age	1SE(int)
	Grain 1	63	62297	101128	1,6	0,1	6,43	0,31	30,3	3,89
	Grain 2	7	9305	7523	1,7	0,2	7,04	0,34	20,6	7,8
	Grain 3	5	6031	8290	1,5	0,3	7,20	0,73	22,2	9,99
	Grain 4	2	6679	2994	1,7	0,2	2,30	0,33	25,09	17,83
	Grain 5	3	12772	2349	2,0	0,7	1,73	0,13	26,16	15,14
	Grain 6	4	18389	2175	1,7		2,27	0,15	18,48	9,26
	Grain 7	7	14705	4760	2,2		3,09	0,17	29,68	11,25
	Grain 8	3	11738	2556	2,5	0,5	1,79	0,15	27,51	15,93
	Grain 9	7	22655	3090	1,7	0,0	1,92	0,22	31	11,85
	Grain 10	42	19418	21629	2,3	0,2	13,29	0,54	31,35	4,88
	Grain 11	36	16192	22233	2,0	0,2	21,77	0,94	19,69	3,31
	Grain 12	4	3343	11965	1,6	0,1	5,64	0,53	40,84	20,51
	Grain 13	5	13110	3814	1,1	0,3	2,06	0,16	35,65	16
	Grain 14	3	7903	3796	1,6	0,1	1,41	0,11	51,78	29,96
	Grain 15	4	13781	2903	2,8	0,6	1,72	0,13	32,5	16,3
	Grain 16	1	11119	899	1,9	0,1	1,52	0,13	11,42	11,43
	Grain 17	5	9796	5104	2,4	0,1	1,40	0,17	70,02	31,6
	Grain 18	6	17007	3528	2,4		1,84	0,16	36,92	15,16
	Grain 19	19	15137	12552	2,3	0,4	9,92	0,55	24,39	5,64
	Grain 20	11	48462	2270	2,3	0,3	1,47	0,12	29,75	9,05
	Grain 21	10	18880	5297	1,5		4,91	0,31	20,8	6,61
	Grain 22	4	10666	3750	2,1		1,56	0,13	46,25	23,21
	Grain 23	67	7852	85329	2,1	0,4	47,07	2,22	34,91	4,34
	Grain 24	5	10414	4801	2,1		3,27	0,58	28,29	12,9
	Grain 25	3	16498	1818	1,7		1,43	0,12	24,51	14,19
	Grain 26	50	10569	47308	2,3	0,6	32,63	1,29	27,94	3,99
	Grain 27	66	32141	20535	1,9	0,2	15,13	0,68	26,15	3,27
	Grain 28	4	9992	4003	1,9	0,0	2,92	0,19	26,42	13,24
	Grain 29	53	26978	19646	2,2	0,2	13,2	0,54	28,67	3,98
	Grain 30	9	13529	6652	2,0	0,5	4,73	0,3	27,1	9,07
	Grain 31	3	21259	1411	2,0	0,0	1,24	0,1	21,94	12,7
	Grain 32	29	20007	14495	1,7	0,2	9,34	0,47	29,9	5,6
	Grain 33	2	11701	1709	1,2		1,31	0,12	25,15	17,82
	Grain 34	2	12498	1600	1,4		1,49	0,12	20,71	14,66
		544	562823	443915	1,9		**Central Age**	**28,57**	**1,24**	**MSWD**	**0,62**
							Pooled age	**26,84**	**1,38**	**p(x2)**	**0,95**
										Disp	**0,0068**
				6,94	0,39						

YSF-AFT3		Tracks	Area (μm²)	Density (tracks/cm2)	Average DPar(μmm)	DPar Std Deviation	U238 (ppm)	2SE(int)	Age	1SE(int)
	Grain 1	54	30244	178548	2,6	0,1	9,92	0,45	34,7	4,78
	Grain 2	31	19755	156922	2,0	0,7	9,84	0,51	30,7	5,57
	Grain 3	36	15790	227992	3,0	0,3	13,62	0,65	32,2	5,43
	Grain 4	45	20993	214357	2,6	0,3	15,71	0,81	26,3	3,98
	Grain 5	54	14403	374922	1,8	0,3	27,78	1,17	26	3,58
	Grain 6	62	21733	285280	2,0	0,3	17,59	0,78	31,2	4,03
	Grain 7	101	23402	431587	1,8	0,2	26,33	1,34	31,6	3,24
	Grain 8	16	7718	207308	2,2	0,3	11,79	0,50	33,9	8,5
	Grain 9	14	8398	166706	2,8	0,3	11,35	0,51	28,3	7,59
	Grain 10	22	9381	234517	2,4	0,3	14,34	0,72	31,5	6,76
	Grain 11	32	10324	309957	2,4	0,1	12,65	0,59	47,1	8,41
	Grain 12	18	9261	194363	2,7	0,2	11,73	0,51	31,9	7,55
	Grain 13	38	12338	307992	1,6	0,0	21,83	0,90	27,2	4,45
	Grain 14	68	30050	226290	2,7	0,1	13,49	0,64	32,3	3,99
	Grain 15	39	15893	245391	2,4	0,1	15,68	0,68	30,2	4,87
	Grain 16	18	7344	245098	2,2	0,4	13,02	0,66	36,3	8,59
	Grain 17	32	17114	186981	2,7	0,1	14,15	0,65	25,5	4,54
	Grain 18	49	21277	230296	2,4	0,1	14,50	0,70	30,6	4,43
	Grain 19	28	11401	245592	1,9	0,3	14,43	0,73	32,8	6,25
	Grain 20	11	5374	204689	2,5	0,1	9,40	0,43	41,9	12,67
	Grain 21	40	12398	322633	2,1	0,0	21,55	0,95	28,8	4,6
	Grain 22	22	7864	279756	3,2	0,1	17,91	1,02	30,1	6,47
	Grain 23	19	13690	138787	2,0	0,4	10,84	0,48	24,7	5,69
	Grain 24	23	9558	240636	2,2	0,2	14,33	0,68	32,3	6,79
	Grain 25	33	19778	166852	3,0	0,0	8,84	0,50	36,3	6,41
	Grain 26	16	12157	131611	2,3	0,3	7,28	0,42	34,8	8,76
	Grain 27	38	10766	352963	2,0	0,5	18,24	0,82	37,3	6,1
	Grain 28	25	7883	317138	2,6	0,3	19,20	0,83	31,8	6,4
	Grain 29	34	7887	431089	1,6	0,1	27,76	1,34	29,9	5,18
	Grain 30	32	15561	205642	2,0	0,2	10,66	0,55	37,1	6,64
	Grain 31	37	14548	254330	2,5	0,1	15,64	0,74	31,3	5,2
	Grain 32	34	8963	379337	2,4	0,4	19,43	0,86	37,6	6,5
	Grain 33	27	9585	281690	3,2	0,3	16,06	0,76	33,8	6,55
	Grain 34	41	12360	331715	2,6	0,3	20,41	0,86	31,3	4,93
	Grain 35	19	12251	155089	2,1	1,1	9,72	0,52	30,7	7,1
	Grain 36	22	10258	214467	2,8		12,51	0,62	33	7,09
	Grain 37	16	7312	218818	2,8	0,2	12,94	0,62	32,6	8,18
	Grain 38	21	10578	198525	3,1	0,1	10,35	0,52	36,9	8,11
	Grain 39	14	7689	182078	2,2	0,4	10,05	0,44	34,9	9,36
	Grain 40	46	18417	249769	2,2	0,3	17,44	0,85	27,6	4,12
	Grain 41	72	18428	390710	2,8	0,5	16,99	0,85	44,3	5,33
	Grain 42	45	21984	204694	2,7	0,5	13,06	0,61	30,2	4,56
	Grain 43	63	30309	207859	2,5	0,4	12,80	0,61	31,3	4,01
		1507	612417	10730981	2,4			**Central Age**	**32,1**	**0,84**
								Pooled Age	**31,6**	**1,1**

MSWD	**0,65**
p(x2)	**0,96**
Disp	**0,0049**

YSF-AFT4	Grain	Tracks	Area (µm2)	Density (tracks/cm2)	Average DPar(µmm)	DPar Std Deviation	U238 (ppm)	2SE	Age	1SE(int)
	Grain01	29	20240	143200	2,97	0,44	8,96	0,73	30,8	5,86
	Grain02	19	7753	245100	2,83	0,39	12,49	0,94	37,78	8,78
	Grain03	11	4783	230000	2,75	0,38	9,81	0,66	45,11	13,69
	Grain04	10	5933	168500		0,00	9,07	0,55	35,78	11,37
	Grain05	8	8456	94610		0,00	5,70	0,43	31,97	11,37
	Grain06	25	12030	207800	2,76	0,31	9,76	0,63	40,98	8,3
	Grain07	19	9387	202400	1,94	0,88	12,30	0,65	31,7	7,32
	Grain08	18	9170	196300	1,63	0,96	13,21	0,78	28,63	6,8
	Grain09	9	12730	70710	1,18	0,32	4,74	0,35	28,74	9,64
	Grain10	8	10040	79710	1,54	0,57	6,55	0,52	23,45	8,34
	Grain11	10	12620	79230		0,00	6,45	0,50	23,68	7,54
	Grain12	14	13260	105600	1,51	0,39	6,40	0,51	31,78	8,59
	Grain13	36	9777	368200	2,13	0,50	15,28	0,91	46,36	7,85
	Grain14	57	8685	656300	1,88	0,81	20,98	1,35	60,12	8,2
	Grain15	9	9238	97420	1,61	0,00	4,79	0,35	39,15	13,13
	Grain16	9	4985	180600	1,8	0,00	5,98	0,50	58,04	19,5
	Grain17	9	4573	196800	1,56	0,26	8,58	0,47	44,14	14,76
	Grain18	20	10710	186700	1,47	0,37	5,76	0,45	62,3	14,14
	Grain19	26	16700	155700	1,65	0,62	4,65	0,30	64,33	12,79
	Grain20	15	5873	255400	1,78	0,53	8,05	0,50	60,98	15,86
	Grain21	13	9066	143400	1,16	0,46	6,76	0,44	40,83	11,4
	Grain22	8	8156	98090	1,62	0,67	3,71	0,32	50,85	18,11
	Grain23	6	8842	67850	1,27	0,38	2,55	0,22	51,18	21,01
	Grain24	10	14720	67920	1,79	0,73	2,49	0,22	52,47	16,75
	Grain25	6	5438	110300	1,33	0,57	4,21	0,28	50,41	20,65
	Grain26	13	10720	121300	1,62	0,62	4,81	0,37	48,50	13,58
	SUM	417	253885	164248	1,8			**Central Age**	**42,33**	**2,63**
								Pooled Age	**40,28**	**3,4**

MSWD	**1,40**
p(x2)	**0,071**
Disp	**17,3**

05 November 2020, Cukurova University Central Research Laboratory, Adana								Data for Tera-Wasserburg plot						Data for Wetherill plot							Dates												
Identifier	Comments	f206c	206Pb	Uppm	Th/U	206Pb/204	1s%	238U/206P	1s%	207Pb/206	1s%	208Pb/206	1s%	207Pb/235U	2s (abs)	206Pb/238U	2s (abs)	Rho	208Pb/232	1s%	207Pb/206Pb	2s (abs)	2ssys (abs)	206Pb/238U	2s (abs)	2ssys (abs)	207Pb/235U	2s (abs)	2ssys (abs)	208Pb/232	2s (abs)	2ssys (abs)	% conc
Z_91500		#YOK	29237	83	0,32	#YOK	#YOK	5,60	9,8	0,07580	24,04	#YOK	#YOK	1,896171759	0,152877987	0,17985137	0,003023728	0,32	0,056923	28,046	1023,2	955,7	85,1	1065,5	186,1	16,5	1060,9	598,2	53,1	1117	611	54	100,4
Z_91500		#YOK	32010	92	0,33	#YOK	#YOK	5,58	10,2	0,07512	26,20	#YOK	#YOK	1,984683959	0,166038494	0,18025475	0,003109721	0,34	0,058859	24,26725	1037,9	996,6	88,1	1067,6	197,6	17,0	1074,5	597,4	51,4	1154	545	47	99,4
Z_91500		#YOK	24030	85	0,34	#YOK	#YOK	5,62	9,8	0,07434	24,82	#YOK	#YOK	1,970693517	0,158686484	0,17977347	0,00314989	0,27	0,054634	32,73832	995,9	979,7	89,8	1065,0	190,1	17,2	1065,8	560,9	50,8	1072	684	62	99,9
Z_91500		#YOK	22901	83	0,33	#YOK	#YOK	5,63	9,8	0,07446	25,39	#YOK	#YOK	2,14938705	0,217074131	0,17932495	0,003059441	-0,09	0,054211	32,02915	1011,8	962,9	84,1	1062,6	194,6	16,7	1087,3	626,4	53,9	1072	686	59	97,7
Z_91500		#YOK	22189	94	0,34	#YOK	#YOK	5,62	9,9	0,07572	24,93	#YOK	#YOK	1,837454851	0,142971988	0,1796427	0,003118595	0,41	0,056017	30,84327	1014,5	1000,2	86,4	1064,3	197,5	17,0	1048,0	618,7	53,3	1099	661	57	101,5
Z_91500		#YOK	22282	94	0,34	#YOK	#YOK	5,63	10,1	0,07519	25,40	#YOK	#YOK	1,868045497	0,178865737	0,17928329	0,003261703	0,20	0,058469	31,34829	1035,3	968,8	88,8	1062,3	198,2	17,8	1023,0	589,4	52,9	1146	697	63	103,8
Z_91500		#YOK	19943	83	0,34	#YOK	#YOK	5,62	10,5	0,07633	26,18	#YOK	#YOK	1,967720386	0,181918121	0,17945048	0,003388014	0,31	0,052648	34,07456	1051,3	1020,6	91,3	1063,1	210,2	18,5	1070,2	661,2	58,2	1034	687	60	99,3
Z_91500		#YOK	20865	86	0,34	#YOK	#YOK	5,59	9,8	0,07568	26,31	#YOK	#YOK	1,962195029	0,14779768	0,1801795	0,002964169	0,28	0,053653	29,22202	1048,7	981,5	86,4	1067,3	187,8	16,2	1064,1	551,4	47,5	1054	601	52	100,3
Z_91500		#YOK	19161	87	0,33	#YOK	#YOK	5,60	9,9	0,07482	26,11	#YOK	#YOK	1,859022399	0,179966846	0,18030901	0,003673723	0,35	0,058226	33,40625	1023,3	1007,7	106,2	1068,0	192,3	20,0	1026,7	557,9	58,2	1141	740	77	104,0
Z_91500		#YOK	19193	93	0,33	#YOK	#YOK	5,61	9,6	0,07376	25,25	#YOK	#YOK	1,968801983	0,245927941	0,17981196	0,004049256	0,24	0,063049	29,755	1045,5	932,3	112,2	1065,3	189,9	22,1	1052,3	633,1	73,6	1233	715	83	101,2
Z_91500		#YOK	20825	104	0,33	#YOK	#YOK	5,58	10,7	0,07719	24,71	#YOK	#YOK	2,080418631	0,22501326	0,18035538	0,004454795	0,45	0,050182	27,37612	1076,6	957,3	114,4	1068,1	205,9	24,3	1097,8	598,4	70,5	988	528	62	97,3
Z_91500		#YOK	21460	107	0,32	#YOK	#YOK	5,58	9,6	0,07702	24,24	#YOK	#YOK	2,190537682	0,30182226	0,18067911	0,004234775	0,16	0,049695	29,65611	1046,1	973,9	119,0	1070,0	189,0	23,1	1118,2	670,7	81,9	992	605	74	95,7
Z_GJ1		#YOK	58424	269	0,03	#YOK	#YOK	10,30	9,4	0,06110	24,45	#YOK	#YOK	0,862726016	0,06706532	0,0979505	0,00201569	0,42	0,030364	51,12698	731,2	876,0	108,6	602,2	106,5	11,8	618,9	320,6	35,6	602	610	68	97,3
Z_GJ1		#YOK	63086	330	0,03	#YOK	#YOK	10,34	12,4	0,06088	23,01	#YOK	#YOK	0,790790564	0,075119747	0,09813207	0,003643215	0,53	0,030753	60,48841	682,8	851,6	140,0	603,1	140,2	21,4	582,5	274,4	41,8	609	724	110	103,5
Z_GJ1		#YOK	59867	293	0,03	#YOK	#YOK	10,28	9,1	0,05982	23,04	#YOK	#YOK	0,800719155	0,044245442	0,09775639	0,001624522	0,48	0,031202	56,25018	696,2	771,8	73,6	601,0	111,1	9,5	594,1	299,9	25,7	618	686	59	101,2
Z_GJ1		#YOK	50874	285	0,03	#YOK	#YOK	10,33	10,4	0,06043	23,71	#YOK	#YOK	0,806438045	0,047860523	0,09786686	0,001721066	0,53	0,030384	66,60626	752,8	753,6	73,2	601,6	117,8	10,1	591,9	314,6	27,0	601	791	68	101,6
Z_GJ1		#YOK	50293	284	0,03	#YOK	#YOK	10,28	8,9	0,06073	23,06	#YOK	#YOK	0,83369015	0,052781203	0,09769982	0,001631935	0,57	0,029931	70,65416	736,4	784,6	76,9	600,7	109,6	9,6	606,1	330,1	28,8	592	825	72	99,1
Z_GJ1		#YOK	50884	296	0,03	#YOK	#YOK	10,28	10,9	0,06005	21,42	#YOK	#YOK	0,820558063	0,049211615	0,09812881	0,001865051	0,50	0,032234	66,70815	660,0	763,4	74,1	603,2	121,3	10,9	600,6	306,4	27,6	637	835	75	100,4
Z_GJ1		#YOK	48863	285	0,03	#YOK	#YOK	10,32	9,4	0,06048	23,96	#YOK	#YOK	0,797481012	0,051362186	0,09775061	0,001625631	0,50	0,030903	69,84047	725,8	803,0	79,1	601,0	108,3	9,5	586,7	324,0	28,5	611	842	74	102,4
Z_GJ1		#YOK	48078	307	0,03	#YOK	#YOK	10,31	10,8	0,05966	24,77	#YOK	#YOK	0,804432901	0,055849889	0,09806862	0,002078977	0,54	0,033461	62,6823	699,9	835,5	94,0	602,8	122,0	12,2	592,1	317,7	31,8	661	819	82	101,8
Z_GJ1		#YOK	44587	270	0,03	#YOK	#YOK	10,33	9,5	0,06155	24,58	#YOK	#YOK	0,853306319	0,066383803	0,09768256	0,001912961	0,47	0,027814	66,45318	767,5	815,7	94,2	600,6	108,8	11,2	617,0	357,5	36,9	551	723	75	97,3
Z_GJ1		#YOK	44528	292	0,03	#YOK	#YOK	10,27	9,2	0,05989	23,36	#YOK	#YOK	0,79366644	0,0421376	0,09798184	0,001651314	0,47	0,031639	70,0437	658,6	820,3	77,9	602,3	110,9	9,7	590,7	284,6	24,9	625	864	75	102,0
Z_GJ1		#YOK	43964	284	0,03	#YOK	#YOK	10,33	9,5	0,06094	25,54	#YOK	#YOK	0,83863897	0,056827398	0,09771004	0,001720889	0,40	0,029998	74,44907	759,9	822,5	85,3	600,7	109,7	10,1	604,9	329,2	30,3	593	872	80	99,3
Z_GJ1		#YOK	43185	288	0,03	#YOK	#YOK	10,31	9,5	0,06120	24,15	#YOK	#YOK	0,826710292	0,050248944	0,09791529	0,001597329	0,38	0,032095	71,38276	746,2	809,5	77,2	602,0	109,3	9,4	602,9	329,9	28,3	634	893	77	99,8
Z_GJ1		#YOK	42697	286	0,03	#YOK	#YOK	10,27	9,9	0,05976	22,70	#YOK	#YOK	0,812016576	0,047080627	0,09782144	0,001670353	0,54	0,029335	74,04726	706,1	792,1	76,2	601,4	113,9	9,8	592,4	301,7	26,0	580	847	73	101,5
Z_GJ1		#YOK	41874	288	0,03	#YOK	#YOK	10,31	10,6	0,05985	23,89	#YOK	#YOK	0,821759422	0,047753013	0,09763736	0,001737639	0,53	0,031301	69,44367	697,3	800,6	76,3	600,3	119,1	10,2	597,6	303,2	26,0	619	846	73	100,4
Z_GJ1		#YOK	41413	286	0,03	#YOK	#YOK	10,31	10,0	0,06111	24,10	#YOK	#YOK	0,806056293	0,041915891	0,09799732	0,001698407	0,47	0,030216	72,52592	742,1	811,8	77,4	602,4	115,7	10,0	597,3	285,9	24,6	597	853	73	100,9
Z_GJ1		#YOK	40307	290	0,03	#YOK	#YOK	10,33	10,4	0,05977	24,59	#YOK	#YOK	0,831372208	0,046455978	0,0978286	0,001727616	0,22	0,034045	76,6429	715,2	805,8	77,5	601,4	118,2	10,1	603,8	290,6	24,9	670	1014	87	99,6
Z_GJ1		#YOK	39594	285	0,03	#YOK	#YOK	10,29	9,8	0,06111	25,10	#YOK	#YOK	0,799551001	0,044476268	0,09793568	0,001686939	0,47	0,028021	87,70968	781,9	794,3	77,5	602,0	115,4	9,9	590,0	293,8	25,2	553	959	82	102,0
Z_GJ1		#YOK	38018	292	0,03	#YOK	#YOK	10,30	9,5	0,06027	24,29	#YOK	#YOK	0,820367219	0,057292684	0,09795103	0,001789139	0,44	0,031591	92,40062	757,0	770,4	83,6	602,2	110,5	10,5	595,0	325,9	30,9	621	1127	107	101,2
Z_GJ1		#YOK	37336	281	0,03	#YOK	#YOK	10,32	8,8	0,06047	25,54	#YOK	#YOK	0,811379886	0,059108242	0,09765956	0,001705861	0,34	0,029429	82,60666	745,1	817,5	91,4	600,5	100,6	10,0	590,5	320,0	31,8	581	947	94	101,7
Z_GJ1		#YOK	37567	290	0,03	#YOK	#YOK	10,32	10,3	0,06056	23,22	#YOK	#YOK	0,818952706	0,050951552	0,09773737	0,001796249	0,48	0,033498	70,32891	725,4	781,6	74,5	600,8	123,3	10,5	594,3	325,9	27,8	672	947	81	101,1
Z_GJ1		#YOK	37381	287	0,03	#YOK	#YOK	10,22	10,3	0,05986	25,01	#YOK	#YOK	0,811989676	0,05300721	0,09815298	0,001766465	0,41	0,028958	69,10177	718,4	825,0	80,9	603,3	119,6	10,4	590,0	329,0	28,5	573	783	68	102,3
Z_GJ1		#YOK	36695	285	0,03	#YOK	#YOK	10,23	8,7	0,06102	23,60	#YOK	#YOK	0,847025849	0,048202815	0,09805955	0,001492494	0,39	0,033715	74,74015	700,5	804,9	74,1	602,8	102,1	8,8	615,3	311,2	26,7	664	982	84	98,0
Z_GJ1		#YOK	36820	286	0,03	#YOK	#YOK	10,29	9,5	0,06042	25,14	#YOK	#YOK	0,786284724	0,045627756	0,09742359	0,001665279	0,19	0,028516	75,56099	728,8	851,7	83,1	600,4	116,5	10,1	589,7	317,0	27,5	564	841	73	101,8
Z_GJ1		#YOK	38328	306	0,03	#YOK	#YOK	10,25	10,5	0,05973	23,16	#YOK	#YOK	0,78971714	0,053755473	0,09825598	0,00224663	0,50	0,03189	76,54806	675,0	799,2	91,7	603,9	125,9	13,2	585,3	295,7	31,0	629	952	100	103,2
Z_GJ1		#YOK	36380	274	0,03	#YOK	#YOK	10,33	9,8	0,06057	22,84	#YOK	#YOK	0,839865982	0,051325652	0,09770098	0,001858784	0,41	0,029901	74,35697	694,2	798,7	85,1	600,7	111,8	10,9	609,2	282,3	27,5	591	870	85	98,6
Z_GJ1		#YOK	38040	289	0,03	#YOK	#YOK	10,30	9,9	0,05992	24,75	#YOK	#YOK	0,808242095	0,051794118	0,09781772	0,001641822	0,48	0,029382	76,26034	722,4	815,2	78,8	601,4	112,3	9,6	587,9	329,8	28,3	581	874	75	102,3
Z_GJ1		#YOK	37444	286	0,03	#YOK	#YOK	10,32	9,9	0,06118	24,82	#YOK	#YOK	0,818921629	0,051475443	0,09779823	0,001652478	0,47	0,032854	72,66924	741,8	812,7	76,8	601,2	113,1	9,7	598,0	335,1	28,7	648	929	80	100,5
Z_GJ1		#YOK	37378	287	0,03	#YOK	#YOK	10,30	10,3	0,06036	23,97	#YOK	#YOK	0,818970488	0,0549458	0,0977873	0,001823273	0,33	0,030348	78,07669	763,0	753,1	73,8	601,1	124,9	10,7	593,0	339,1	29,1	599	924	79	101,4
Z_GJ1		#YOK	37291	290	0,03	#YOK	#YOK	10,30	10,5	0,06023	24,78	#YOK	#YOK	0,817423341	0,053681527	0,09819543	0,00187187	0,53	0,031139	74,27363	732,7	826,0	82,6	603,5	124,0	11,0	593,5	323,0	28,6	615	901	80	101,7
Z_GJ1		#YOK	35082	275	0,03	#YOK	#YOK	10,33	10,2	0,06003	25,26	#YOK	#YOK	0,823680611	0,059234458	0,09748214	0,002017456	0,33	0,028494	73,29637	735,9	833,4	99,6	599,4	113,0	11,8	598,5	306,0	32,1	564	818	86	100,1
Z_GJ1		#YOK	36009	296	0,03	#YOK	#YOK	10,34	10,8	0,06068	23,89	#YOK	#YOK	0,800160864	0,04644117	0,0978266	0,001837454	0,52	0,031678	74,93101	670,3	859,5	79,1	601,4	125,6	10,8	586,1	293,2	25,1	625	924	79	102,6
Z_GJ1		#YOK	36011	290	0,03	#YOK	#YOK	10,31	9,2	0,06079	24,27	#YOK	#YOK	0,8325296	0,050915728	0,09783228	0,001563826	0,36	0,030639	81,88424	779,4	763,6	75,2	601,5	106,5	9,2	602,6	315,3	27,1	604	977	84	99,8
Z_GJ1		#YOK	35497	285	0,03	#YOK	#YOK	10,27	10,2	0,06007	24,29	#YOK	#YOK	0,807664755	0,048502871	0,09813476	0,001782311	0,46	0,032508	77,62142	727,8	801,0	79,7	603,2	118,9	10,5	593,4	312,9	27,5	641	978	86	101,7
Z_GJ1		#YOK	36209	311	0,03	#YOK	#YOK	10,30	10,3	0,06051	25,31	#YOK	#YOK	0,796179549	0,059698661	0,09805018	0,002018274	0,55	0,031136	78,81223	713,0	849,7	95,0	602,7	117,2	11,8	581,9	318,4	32,2	614	959	97	103,6
Z_GJ1		#YOK	33377	266	0,03	#YOK	#YOK	10,31	8,4	0,06019	27,40	#YOK	#YOK	0,844195117	0,085942798	0,09738454	0,002032168	0,52	0,028435	86,14074	736,2	872,7	115,6	598,9	101,3	11,9	603,5	377,1	44,4	561	956	113	99,2
Z_GJ1		#YOK	34231	289	0,03	#YOK	#YOK	10,32	9,9	0,06078	23,88	#YOK	#YOK	0,82474643	0,053606068	0,0976304	0,001828548	0,42	0,028204	87,49476	764,6	755,7	76,7	600,2	119,4	10,7	597,7	323,2	29,0	556	964	87	100,4
Z_GJ1		#YOK	33832	286	0,03	#YOK	#YOK	10,24	9,9	0,06007	22,69	#YOK	#YOK	0,809285453	0,055550138	0,0981572	0,001827326	0,41	0,034197	75,15739	671,6	798,4	77,9	603,3	119,9	10,7	588,1	334,2	29,9	674	998	89	102,6
Z_GJ1		#YOK	33984	306	0,03	#YOK	#YOK	10,27	9,5	0,06069	21,10	#YOK	#YOK	0,803262134	0,046490644	0,09798087	0,001970597	0,39	0,033697	75,43674	688,7	705,0	78,3	602,3	111,6	11,6	591,0	251,0	26,0	681	1033	107	101,9
Z_GJ1		#YOK	32064	270	0,03	#YOK	#YOK	10,32	10,0	0,06000	22,86	#YOK	#YOK	0,842775211	0,073365632	0,09787543	0,001977245	0,32	0,028275	85,06315	695,6	758,2	84,8	601,7	113,7	11,6	604,2	356,4	36,4	574	979	100	99,6
Z_GJ1		#YOK	33705	306	0,03	#YOK	#YOK	10,27	9,5	0,05974	23,85	#YOK	#YOK	0,785255345	0,05707501	0,09796951	0,001925747	0,46	0,031787	86,21542	697,0	805,2	90,6	602,3	111,9	11,3	580,7	323,4	32,7	626	1066	108	103,7
Z_GJ1		#YOK	32091	277	0,03	#YOK	#YOK	10,32	8,9	0,06163	24,59	#YOK	#YOK	0,849301363	0,060475576	0,09761269	0,00177806	0,50	0,028981	86,00227	777,7	816,9	95,0	600,2	101,2	10,4	616,8	325,4	33,6	572	967	100	97,3
Z_GJ1		#YOK	32849	288	0,03	#YOK	#YOK	10,30	9,9	0,06048	25,34	#YOK	#YOK	0,822328384	0,058480774	0,09783984	0,001717214	0,51	0,029393	82,51904	710,5	871,5	87,1	601,5	111,7	10,1	594,7	340,5	30,7	580	946	85	101,2
Z_GJ1		#YOK	32574	287	0,03	#YOK	#YOK	10,29	9,7	0,06022	23,15	#YOK	#YOK	0,806563043	0,052664554	0,09790125	0,001639403	0,37	0,032144	70,1216	666,2	792,9	73,6	601,9	111,9	9,6	587,3	321,9	27,7	635	879	76	102,5
Z_Plesovice		#YOK	47666	563	0,08	#YOK	#YOK	18,83	10,5	0,05418	25,19	#YOK	#YOK	0,40410863	0,025384494	0,05368776	0,000963427	0,59	0,017762	41,62991	634,0	702,2	76,2	337,0	67,5	5,9	339,5	203,8	17,8	355	293	26	99,3
Z_Plesovice		#YOK	45728	543	0,08	#YOK	#YOK	18,72	10,3	0,05314	27,92	#YOK	#YOK	0,402220104	0,027722367	0,05385555	0,001022033	0,60	0,018647	46,87083	651,9	747,6	84,6	338,1	70,7	6,2	337,2	219,9	19,4	373	346	31	100,2
Z_Plesovice		#YOK	38307	539	0,08	#YOK	#YOK	18,74	9,6	0,05301	25,93	#YOK	#YOK	0,388825158	0,027691972	0,05369006	0,000998984	0,60	0,018946	42,23353	621,7	685,8	86,4	337,1	61,4	6,1	328,6	198,2	19,7	379	317	32	102,6
Z_Plesovice		#YOK	37552	557	0,09	#YOK	#YOK	18,85	9,1	0,05609	26,35	#YOK	#YOK	0,38815216	0,03008389	0,05330451	0,00120353	0,49	0,019254	43,26634	643,5	812,2	113,7	334,7	62,1	7,4	333,3	193,7	23,0	385	330	39	100,4
Z_Plesovice		#YOK	40701	566	0,09	#YOK	#YOK	18,89	9,9	0,05554	25,14	#YOK	#YOK	0,403595564	0,02587675	0,05343328	0,000926689	0,29	0,017458	45,33471	690,8	664,8	73,4	335,5	62,9	5,7	339,2	202,6	18,3	349	314	28	98,9
Z_Plesovice		#YOK	44950	621	0,09	#YOK	#YOK	18,72	10,0	0,05400	24,52	#YOK	#YOK	0,397478501	0,024230042	0,05394368	0,000925488	0,55	0,01698	41,10934	615,7	711,7	75,9	338,6	66,0	5,7	334,8	200,2	17,2	340	277	24	101,1
Z_Plesovice		#YOK	42329	618	0,09	#YOK	#YOK	18,77	9,6	0,05410	23,82	#YOK	#YOK	0,410686602	0,025185985	0,05374761	0,000947773	0,56	0,016254	44,88428	583,7	702,4	79,5	337,4	61,6	5,8	344,9	189,5	17,8	325	290	27	97,8
Z_Plesovice		#YOK	41128	615	0,09	#YOK	#YOK	18,76	9,0	0,05436	26,22	#YOK	#YOK	0,394367721	0,023107111	0,053637	0,000851383	0,54	0,01763	44,96008	675,3	708,0	77,2	336,7	60,5	5,2	333,0	191,7	16,5	353	314	27	101,1
Z_Plesovice		#YOK	44026	667	0,09	#YOK	#YOK	18,64	8,9	0,05782	23,72	#YOK	#YOK	0,436590213	0,033312977	0,0540662	0,001109247	0,41	0,01561	36,33172	664,2	758,2	101,3	339,4	58,0	6,8	363,1	197,2	23,1	313	225	26	93,5
Z_Plesovice		#YOK	43715	690	0,09	#YOK	#YOK	18,71	9,6	0,05379	24,51	#YOK	#YOK	0,395122935	0,021693672	0,05393517	0,000887774	0,48	0,015415	38,55227	627,7	659,5	70,7	338,6	63,3	5,4	334,0	182,3	15,6	309	236	20	101,4
Spot #97	YSF1_1	#YOK	2136	127	0,35	#YOK	#YOK	78,00	13,1	0,05865	54,13	#YOK	#YOK	0,111594025	0,012108925	0,01301729	0,000311836	0,17	0,004483	100,864	1066,2	1276,8	143,6	83,4	23,1	2,0	105,5	125,3	10,7	90	182	16	79,0
Spot #98	YSF1_2	#YOK	3011	186	0,30	#YOK	#YOK	77,74	13,2	0,04820	46,91	#YOK	#YOK	0,089638597	0,009406953	0,01305293	0,000314566	0,10	0,004168	83,81402	763,0	1009,7	123,4	83,6	23,3	2,0	84,5	92,6	7,9	84	140	12	99,0
Spot #99	YSF1_3	#YOK	2495	154	0,29	#YOK	#YOK	80,35	14,7	0,04981	49,70	#YOK	#YOK	0,095659336	0,009821455	0,01270862	0,000316422	0,20	0,003652	94,26651	866,0	1147,5	139,2	81,4	23,5	2,0	92,6	107,2	9,2	74	139	12	87,9
Spot #100	YSF1_4	#YOK	2838	184	0,41	#YOK	#YOK	77,89	12,4	0,07005	39,50	#YOK	#YOK	0,12959519	0,015229405	0,01283665	0,000426631	0,10	0,00582	51,40846	1031,2	1262,0	184,1	82,2	20,3	2,7	122,5	101,3	13,5	117	120	16	67,1
Spot #101	YSF1_5	#YOK	6199	391	0,55	#YOK	#YOK	80,58	12,2	0,04949	35,30	#YOK	#YOK	0,086116691	0,006128767	0,01259109	0,000260666	0,42	0,003766	43,82604	656,1	844,6	101,7	80,7	19,3	1,7	83,3	66,0	5,7	76	66	6	96,8
Spot #102	YSF1_6	#YOK	5666	379	0,45	#YOK	#YOK	80,03	9,3	0,04619	32,86	#YOK	#YOK	0,079846235	0,009158569	0,01259896	0,000326685	0,12	0,003594	56,3484	555,7	713,9	152,2	80,7	14,6	2,1	77,6	60,1	8,6	72	82	12	104,1
Spot #103	YSF1_7	#YOK	4007	256	0,51	#YOK	#YOK	82,31	12,0	0,04667	37,26	#YOK	#YOK	0,08495184	0,00728183	0,01225516	0,000254595	0,11	0,003735	58,92197	569,8	805,4	94,9	78,5	18,9	1,6	82,0	78,2	6,7	75	89	8	95,7
Spot #104	YSF1_8	#YOK	2785	178	0,42	#YOK	#YOK	80,81	12,6	0,04679	46,79	#YOK	#YOK	0,079685123	0,007767865	0,01257095	0,000283303	0,16	0,003284	77,38569	713,6	879,9	112,7	80,5	20,2	1,8	77,1	80,4	7,2	66	102	9	104,5
Spot #105	YSF1_9	#YOK	3997	265	0,37	#YOK	#YOK	80,53	12,5	0,04804	40,38	#YOK	#YOK	0,084020978	0,00734707	0,01251743	0,000279246	0,17	0,003836	71,72863	699,4	835,1	107,8	80,2	19,2	1,8	81,2	73,8	6,8	77	111	10	98,7
Spot #106	YSF1_10	#YOK	7004	460	0,64	#YOK	#YOK	81,34	10,0	0,04865	36,74	#YOK	#YOK	0,080019798	0,00643503	0,01235311	0,000229052	0,20	0,003975	40,29779	693,6	884,0	123,8	79,1	15,6	1,5	77,7	64,1	6,0	80	64	6	101,9
Spot #107	YSF1_11	#YOK	4058	277	0,51	#YOK	#YOK	82,27	13,6	0,04730	38,73	#YOK	#YOK	0,077051534	0,006797484	0,01227171	0,000323576	0,21	0,004196	59,1396	580,5	844,3	117,1	78,6	20,4	2,1	74,9	62,9	6,4	85	100	10	105,0
Spot #108	YSF1_12	#YOK	5486	368	0,52	#YOK	#YOK	81,08	12,7	0,04682	35,58	#YOK	#YOK	0,079250892	0,00649638	0,01249041	0,000294461	0,43	0,003886	55,69269	583,5	809,7	106,3	80,0	20,1	1,9	76,9	64,8	6,0	78	87	8	104,0
Spot #109	YSF1_13	#YOK	2959	199	0,48	#YOK	#YOK	82,49	12,7	0,04848	43,19	#YOK	#YOK	0,079159895	0,008721879	0,01226932	0,00031891	0,26	0,003721	68,07423	701,3	955,8	142,5	78,6	19,6	2,0	76,6	77,6	8,0	75	102	11	102,6
Spot #110	YSF1_14	#YOK	2166	147	0,29	#YOK	#YOK	82,18	13,0	0,04818	48,10	#YOK	#YOK	0,087372822	0,011668814	0,01236773	0,000315401	0,11	0,004351	94,1186	830,7	1077,9	158,9	79,2	19,9	2,0	81,5	94,3	9,5	88	165	17	97,3
Spot #111	YSF1_15	#YOK	1998	134	0,32	#YOK	#YOK	81,47	11,5	0,05140	51,29	#YOK	#YOK	0,090181475	0,011458053	0,01235598	0,000292077	0,08	0,003549	100,3448	889,4	1092,2	141,0	79,2	19,7	1,9	86,2	109,0	10,3	71	143	14	91,8
Spot #112	YSF1_16	#YOK	5211	345	0,40	#YOK	#YOK	80,63	11,1	0,04847	37,08	#YOK	#YOK	0,084289601	0,006875478	0,01251957	0,000272418	0,25	0,003487	61,26901	634,7	837,4	112,9	80,2	18,0	1,7	81,6	66,3	6,4	70	86	8	98,2
Spot #113	YSF1_17	#YOK	2366	171	0,35	#YOK	#YOK	85,51	14,3	0,04847	48,44	#YOK	#YOK	0,077975623	0,010401864	0,01180718	0,000365679	0,16	0,003927	98,31505	782,5	1093,6	170,8	75,7	21,1	2,3	75,3	86,8	9,6	79	155	17	100,5
Spot #114	YSF1_18	#YOK	3150	224	0,45	#YOK	#YOK	82,37	11,8	0,04712	44,86	#YOK	#YOK	0,076501674	0,008072072	0,01227523	0,000311489	0,21	0,003125	90,46164	673,9	898,5	131,1	78,6	19,4	2,0	74,2	73,7	7,5	63	114	12	106,0
Spot #115	YSF1_19	#YOK	2550	178	0,36	#YOK	#YOK	80,23	13,4	0,04579	48,43	#YOK	#YOK	0,079600006	0,008970636	0,0126273	0,000344353	0,25	0,003925	92,58893	717,0	833,2	127,1	80,9	20,8	2,2	77,0	79,2	8,3	79	146	15	105,0
Spot #116	YSF1_20	#YOK	2651	187	0,38	#YOK	#YOK	81,73	13,3	0,04838	45,61	#YOK	#YOK	0,079372085	0,00903896	0,01234432	0,000340192	0,19	0,004532	82,70136	751,9	1089,1	157,2	79,1	20,7	2,2	76,8	79,4	8,3	91	151	16	103,0
Spot #117	YSF1_21	#YOK	3530	254	0,30	#YOK	#YOK	81,41	11,9	0,04772	46,10	#YOK	#YOK	0,077122785	0,008963704	0,01245876	0,000340231	0,34	0,00489	79,42955	814,1	890,2	150,5	79,8	19,2	2,2	74,8	74,2	8,4	98	156	18	106,8
Spot #118	YSF1_22	#YOK	3649	259	0,36	#YOK	#YOK	82,05	14,9	0,05046	42,64	#YOK	#YOK	0,083176565	0,008457524	0,01245976	0,000401104	0,29	0,003669	77,35016	719,8	847,7	119,9	79,8	23,9	2,6	80,5	73,9	7,9	74	114	12	99,2
Spot #119	YSF1_23	#YOK	1819	133	0,27	#YOK	#YOK	82,72	15,8	0,04694	53,12	#YOK	#YOK	0,08085617	0,011680218	0,01231505	0,000421081	0,28	0,004822	126,5803	856,4	999,1	162,1	78,9	25,0	2,7	77,7	99,5	10,7	97	245	26	101,5
Spot #120	YSF1_24	#YOK	6574	473	0,65	#YOK	#YOK	81,22	12,1	0,05303	34,03	#YOK	#YOK	0,086564589	0,006765403	0,01237915	0,00028832	0,32	0,004346	42,1956	678,4	891,5	117,1	79,3	18,0	1,8	83,8	61,6	6,3	88	74	8	94,6
Spot #121	YSF1_25	#YOK	3849	283	0,32	#YOK	#YOK	81,45	13,2	0,04884	37,53	#YOK	#YOK	0,081024744	0,007341989	0,01243889	0,000365264	0,31	0,005029	75,65783	664,6	790,5	119,2	79,7	21,4	2,3	79,8	66,5	7,2	101	153	17	99,9
Spot #122	YSF1_26	#YOK	1420	103	0,30	#YOK	#YOK	82,39	14,4	0,05108	61,16	#YOK	#YOK	0,091242783	0,01472043	0,01239132	0,000365078	0,15	0,003283	148,7103	1011,2	1199,4	167,9	79,4	23,0	2,3	86,5	130,9	13,2	66	196	20	91,7
Spot #123	YSF1_27	#YOK	10146	725	0,34	#YOK	#YOK	78,98	10,1	0,04916	29,58	#YOK	#YOK	0,080942282	0,006278714	0,01274992	0,000293323	0,45	0,004168	44,28079	582,7	671,4	99,0	81,7	17,3	1,9	78,7	54,3	5,9	84	74	8	103,8
Spot #124	YSF1_28	#YOK	1605	118	0,34	#YOK	#YOK	83,19	14,7	0,04656	62,45	#YOK	#YOK	0,080595076	0,012527374	0,01222593	0,000397087	0,20	0,003349	128,3599	802,0	1114,2	169,9	78,3	23,3	2,5	77,3	106,6	11,6	67	173	19	101,3
Spot #125	YSF1_29	#YOK	24087	1114	0,23	#YOK	#YOK	224,62	147,4	0,04722	26,59	#YOK	#YOK	0,066453793	0,004710844	0,01411883	0,002848979	0,30	0,001115	197,8516	490,6	628,2	77,3	90,2	97,6	18,1	65,6	53,2	4,6	22	89	8	137,5
Spot #126	YSF1_30	#YOK	2179	157	0,31	#YOK	#YOK	81,65	11,2	0,04523	49,09	#YOK	#YOK	0,072774413	0,00844697	0,01235433	0,000291926	0,12	0,00427	113,0846	734,5	1023,1	159,8	79,1	17,6	1,9	70,6	74,8	7,9	86	194	20	112,0

238U/235U	137,818
BeamSecondsMa	60
BeamSecondsMe	Laser log
BeamSecondsSen	1000
DefaultFitType	Exponential
FitEndCrop	1
FitStartCrop	1
IndexChannel	U238
MaskChannel	U238
MaskMethod	Laser log
MaskResults	DOĞRU
MaskThreshold	1000
MaskTrim	0
ReferenceMateri	Z_91500
l232	4,95E-11
l235	9,85E-10
l238	1,55E-10